3-24-2016

Localized Plasma Measurement During Instability Modes In a Hall Thruster

David A. Cunningham

Localized Plasma Measurement During Instability Modes In a Hall Thruster

THESIS

David A. Cunningham, Captain, USAF

AFIT-ENY-MS-16-M-203

DEPARTMENT OF THE AIR FORCE
AIR UNIVERSITY

AIR FORCE INSTITUTE OF TECHNOLOGY

Wright-Patterson Air Force Base, Ohio

AFIT-ENY-MS-16-M-203

Localized Plasma Measurement During Instability Modes In a Hall Thruster

THESIS

Presented to the Faculty

Department of Aeronautics and Astronautics

Graduate School of Engineering and Management

Air Force Institute of Technology

Air University

Air Education and Training Command

In Partial Fulfillment of the Requirements for the

Degree of Master of Science in Astronautical Engineering

David A. Cunningham

Captain, USAF

March 2016

AFIT-ENY-MS-16-M-203

Localized Plasma Measurement During Instability Modes In a Hall Thruster

David A. Cunningham
Captain, USAF

Committee Membership:

Carl R. Hartsfield, PhD
Chair

Maj David Liu, PhD
Member

William Hargus, PhD
Member

Abstract

Hall thrusters are a key technology for current and future unmanned satellites, striking a balance between thrust and fuel economy suitable for many mission profiles of interest. Despite their extensive flight heritage and a large body of research, many phenomena occuring in the plasma discharge of Hall thrusters are not well understood. A combination of intrusive and non-intrusive measurement techniques were used to investigate the properties of the exhaust plume of two Hall thrusters and correlate optical characteristics of oscillating modes with the plasma potential and azimuthal current distribution during those modes. A strong trend was found associating the optical emission of spokes with a local increase in plasma potential as measured by an emissive probe, indicating a spoke structure with visible and non-visible regions. Additionally, a consistent phase delay was observed between oscillations in discharge current and Hall current during the breathing mode. A similar delay was not observed between discharge current and optical emission or plasma potential oscillations during the breathing mode. These trends were used to infer a possible plasma structure during breathing and spoke modes.

For my wife.

Acknowledgements

Thanks to my advisors Maj Liu and Dr. Hartsfield, for teaching me about Hall thrusters and how to work in the lab. Thanks to Jamie, Keith, Barry, and Jay for all their support with equipment. Thanks to Connor for taking time out of his research to help me calibrate my sensors.

I would also like to gratefully acknowledge Dr. Mitat Birkan of the Air Force Office of Scientific Research for providing funding and support for this research.

David A. Cunningham

Table of Contents

Page

List of Figures

List of Tables

Localized Plasma Measurement During Instability Modes In a Hall Thruster

I. Introduction

1.1 Background

Hall thrusters represent a unique electric propulsion solution for unmanned satellite missions. First flown in the USSR during the 1970s, Hall thrusters have enjoyed a recent resurgence in domestic flight and research interest with over 200 thrusters flown worldwide [1]. The list of missions includes the Air Force's TacSat 2 and the Advanced Extremely High Frequency system, where a Hall thruster was used to provide the impulse for one satellite's transfer from low Earth orbit to its operational geosynchronous orbit after the main propulsion system failed [1, 2]. The reliability, efficiency, and versatility of Hall thrusters as well as other forms of electric propulsion are major reasons for their continued and increasing use on unmanned satellite systems.

Hall thrusters are capable of moderate to high performance in terms of fuel economy, with specific impulses from 1500 to 2000 seconds common as well as typical power requirements of 0.2 to 4.5 kW [1]. Their typical applications include stationkeeping for geosynchronous communications satellites, attitude control, or as an orbital maneuvering propulsion system if the higher thrust of a chemical rocket is not required. The physics of Hall thrusters gives them the benefit of a higher thrust-to-power ratio than the also popular gridded ion engine. As thruster technology improves, Hall thrusters could see increasing use on small satellite systems to provide reliable propulsion, extending the operational life of a class of satellite vehicles traditionally lacking a means of active orbit maintenance.

1.2 Motivation

Electric propulsion systems such as Hall thrusters are used to provide impulse to spacecraft for attitude control, stationkeeping, or orbital maneuvering. Like a chemical rocket, the efficient operation of an electric system is dependent on the acceleration of the thruster. In a chemical rocket, the energy necessary to cause this acceleration is provided by an oxidation reaction causing hot gases to be ejected from the nozzle, while in electrostatic propulsion systems ions are accelerated through an electric field to the engine exit. Therefore, the examination of ionization processes in electric thrusters is as important as the understanding of the combustion process in chemical rockets, if efficient operation is desired.

There are several ways Hall thruster research impacts the Department of Defense. Onboard propellant storage is a limiting factor on satellite lifetime, and the specific impulse performance of electric propulsion systems such as Hall thrusters make them an attractive option to the spacecraft designer. In addition, the lack of moving parts and high thrust to power ratio of Hall thrusters relative to other forms of electric propulsion means that they are ideal for long-duration missions with a consistent, low-thrust stationkeeping requirement and a surplus of electrical power to drive the thruster. Finally, the mass savings realized due to the fuel performance of Hall thrusters means satellites may have more room for payload and/or lower cost per launch. The improvement of Hall thrusters could lead to longer satellite design lifetimes through reduction in propellant usage, increased reliability through improvement in thruster performance, and lower costs at a system level due to the simplicity of Hall thrusters.

Despite a growing flight heritage and increased research interest in Hall thrusters, the complicated plasma dynamics occuring in the thruster channel and plume remain an active research area. Although performance metrics for thrusters are defined in the average, observed plasma phenomena vary from thruster to thruster and from operating condition to operating condition without a unified physical model of behavior.

A better understanding of the physics of Hall thruster operation can improve their design and performance.

1.3 Scope

The focus of the present research is the observation and characterization of time-dependent plasma structures in a Hall thruster. Although the results may be useful for determining the causes of some types of plasma phenomena, such analysis is outside of the scope of the current effort. As the operation of thrusters in several regimes is relevant to system design, the behavior of the plasma in nominal and low powered conditions is examined. Plasma characteristics measured include the plasma potential measured with an emissive probe, induced magnetic field measured with an array of magnetic sensors, and optical emission measured with a high-speed camera. Analysis of the measured data includes correlation in time of the various signals, as well as extraction of Hall current data from the magnetic field measurements.

1.4 Objectives

Hall thrusters are a key technology for the future of unmanned spaceflight. Due to the high cost of space launch, the length and scope of satellite missions is often limited by the amount of propellant onboard. Since the propulsion system often limits lifespan, an efficient system can increase the design life of satellites and reduce mission cost and complexity. Although Hall thrusters are more efficient in an absolute sense than their chemically powered conterparts, many aspects of their operation are complex and poorly understood. To improve the efficiency of Hall thrusters, it is necessary to identify, characterize, and control phenomena which may impede the energy and propellant supplied to the thruster from conversion into useful thrust. Chief among these phenomena are the oscillations of the plasma. Therefore, the goal of this research is to determine the properties of the plasma in the channel of a Hall thruster in an effort to understand the time-dependent behavior of the discharge. The following objectives are key to accomplishing the research goals:

1. In the plume of a 600 W thruster operating at nominal conditions, correlate non-intrusive visual measurements of plasma emission using a high speed camera and intrusive measurements of plasma potential using an emissive probe at sampling rates up to 500 kHz.
2. In the plume of a 600 W thruster operating at off-nominal conditions, correlate non-intrusive visual measurements of plasma emission using a high speed camera and intrusive measurements of plasma potential using an emissive probe at sampling rates up to 500 kHz.
3. In the plume of a 600 W thruster operating at nominal conditions, correlate non-intrusive visual measurements of plasma emission using a high speed camera and intrusive measurements of the localized magnetic field at sampling rates up to 500 kHz.
4. In the plume of a 600 W thruster operating at off-nominal conditions, correlate non-intrusive visual measurements of plasma emission using a high speed camera and intrusive measurements of the localized magnetic field at sampling rates up to 500 kHz
5. Examine the fidelity of measurements 1-4 in the plume of a 200 W thruster.

II. Background

2.1 Fundamentals of Rocket Propulsion

All rocket propulsion is based on Newton's second law: the time rate of change of the momentum of a system is equal to the sum of the forces applied to that system. This is expressed mathematically as:

$$\mathbf{F} = \dot{\mathbf{p}} \tag{2.1}$$

where $\mathbf{F}$ is the resultant force and $\mathbf{p}$ is the momentum of the system. Now consider the total momentum of a rocket vehicle in free space. The rocket is moving with a velocity $v(t)$ and has a mass $m(t)$. It expels mass at a constant rate $\dot{m}$ and a constant exhaust velocity opposite to its direction of motion v_e. If the system is closed, *i.e.* no mass leaves, the total momentum is [3]:

$$p = m(t)v(t) + \int_0^{m(0)-m(t)} (v(t) - v_e)\, dm \tag{2.2}$$

where each expelled mass element dm is summed over, and each is necessarily moving with a velocity $v - v_e$. Since the mass flow rate is constant and negative, the integral over time is:

$$p = m(t)v(t) - \int_0^t \dot{m}\,(v(t) - v_e)\, dt. \tag{2.3}$$

Figure 2.1 shows the system under consideration.

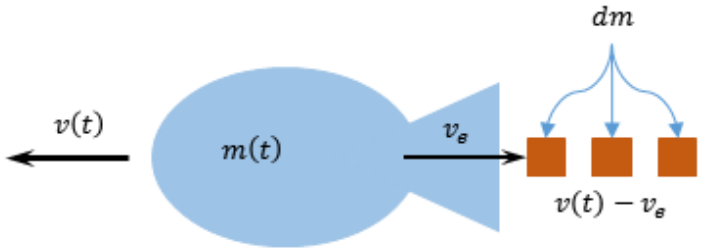

Figure 2.1: Rocket system.

Now, Newton's second law says in the absence of external forces, the net change in momentum over time is zero. This is true in the case of Fig. 2.1 if any forces due to the pressure of the rocket exhaust are neglected, a reasonable assumption in the case of very low pressure electric systems such as the Hall thruster. Thus, Equation 2.3 is differentiated in time and inserted into Eq. 2.1 to obtain:

$$\dot{p} = \dot{m}v(t) + m(t)\dot{v} - \dot{m}v(t) + \dot{m}v_e. \tag{2.4}$$

Since the total change in momentum is zero,

$$m(t)\dot{v} = -\dot{m}v_e \tag{2.5}$$

meaning at each instant the vehicle experiences a force equal to the mass flow rate times the exhaust velocity. This force is defined as the thrust:

$$T \equiv v_e\dot{m} \tag{2.6}$$

and it is noted if a pressure force were present v_e would incorporate this performance change and become an equivalent exhaust velocity. Now, if the time dependence is eliminated from Eq. 2.5 it becomes

$$\int_{v_0}^{v_f} dv = -I_{sp}g_0 \int_{m_0}^{m_f} \frac{dm}{m} \tag{2.7}$$

where the specific impulse I_{sp} is defined as the impulse provided per unit weight of fuel at the surface of Earth:

$$I_{sp} \equiv \frac{T}{g_0\dot{m}} = \frac{v_e}{g_0} \tag{2.8}$$

carrying out the integration, the total change in velocity for an amount of mass expelled is

$$\Delta v = I_{sp}g_0 \ln\left(\frac{m_0}{m_f}\right) \tag{2.9}$$

where $\Delta v = v_f - v_0$. This is the ideal rocket equation in free space [3].

Equations 2.6, 2.8, and 2.9 enable the conversion from propulsion system performance in terms of I_{sp} and thrust to mission performance in terms of the Δv avaliable for a given propellant mass and maneuver length.

2.2 Selected Plasma Fundamentals

Fundamentally, plasma is the state of matter arising when the atoms or molecules in a material can no longer retain enough electrons to remain neutrally charged. In this state, the material dissociates into one or more electrically charged species. The free motion of the ions and electrons is reminiscent of the fluid motion of a gas, but the charge carried by the ion and electron populations give rise to various complicated and useful phenomena. A few relevant behaviors of plasma are detailed here.

2.2.1 Quasineutrality. Consider a plasma composed of an equal number of electrons and ions in a vessel: assuming they do not recombine, what configuration will they assume? Neglecting the regions near the walls, the minimum energy configuration allowable is uniform distribution throughout the vessel. This means any volume of the plasma large enough to contain a statistical ensemble of elementary particles will have no net charge. This property is known as quasineutrality of plasma [4]. Deviations from quasineutrality establish fields within plasmas, tending to restore quasineutrality over time following the minimum energy argument. For the number density of ions n_i and the number density of electrons n_e, quasineutrality is expressed mathematically:

$$n_i \approx n_e \approx n. \tag{2.10}$$

If a nonuniformity exists, the field opposing it in any suitably sized volume is given by Gauss's Law [1, 5]:

$$\nabla \cdot \mathbf{E} = \frac{\rho}{\epsilon} = \frac{e^-}{\epsilon}(n_e - n_i) \tag{2.11}$$

where $\mathbf{E}$ is the electric field, ρ is charge density, e^- is the charge of an electron and ϵ is the local permittivity of the plasma.

2.2.2 Velocity Distribution and Temperature. Just as in a gas, kinetic motion of particles is a major characteristic of plasma behavior. As such, particles in a plasma often but not always take on a Maxwellian velocity distribution. In one dimension, this is [4]:

$$f(v) = A \exp\left(-\frac{mv^2}{2kT}\right) \tag{2.12}$$

where m is particle mass, v is velocity, T is temperature, and k is Boltzmann's constant. Equation 2.12 describes a distribution, f returns the probability a random particle will have velocity v. The number density is defined as:

$$n = \int_{-\infty}^{\infty} f(v)dv \tag{2.13}$$

leading to the definition of the constant A in Eq. 2.12:

$$A = n\left(\frac{m}{2\pi kT}\right)^{1/2}. \tag{2.14}$$

Now two more quantities are defined; the thermal velocity $v_{th} = \sqrt{2kT/m}$ and the average energy [4]:

$$E_{av} = \frac{\frac{1}{2}\int_{-\infty}^{\infty} mv^2 f(v)dv}{\int_{-\infty}^{\infty} f(v)dv} = \frac{1}{2}kT \tag{2.15}$$

so, the temperature of a plasma species is a measure of its kinetic energy as well as the parameter describing the variance of its velocity distribution. Note that in three dimensions the average energy is [4]:

$$E_{av} = \frac{3}{2}kT. \tag{2.16}$$

2.2.3 Sheaths and Debye Length. Consider again a vessel containing plasma. Assuming it is a conductor held at a potential above the plasma, near the walls electrons will experience an attractive force due to the electric field established by the potential. These attracted electrons will still undergo motion due to their kinetic velocity depending on the electron temperature, and as the distance from the wall

increases the attractive force experienced by any electron will decrease due to shielding from the negative charge accumulation near the wall. The combination of these two effects causes the potential to decrease as distance from the wall increases. This region of nonuniform potential is a sheath. Sheaths form at the edges of a plasma as well as around any charge introduced into a plasma where the electrons are "thermalized," *i.e.* collisions between electrons are frequent enough to allow consideration of their velocities as a distribution. The length the potential takes to decrease by a value of $1/e$ in the limit $e^{-}\phi_{wall} \ll kT_e$ is termed the Debye length and is given by the formula [1]:

$$\lambda_D = \sqrt{\frac{\epsilon_0 k T_e}{n e^{-2}}} \tag{2.17}$$

where ϵ_0 is the permittivity of free space. Sheaths in plasmas are generally assumed on the order of a few Debye lengths long, and most plasma dynamics theory assumes the characteristic length of the plasma is much larger than the Debye length [4].

2.2.4 Larmor Radius and Cyclotron Frequency. In the presence of electric and magnetic fields, particles obey the Lorentz force equation presented in Eq. 2.18 [1]:

$$\mathbf{F} = m_p \frac{d\mathbf{v_p}}{dt} = q_p \left(\mathbf{E} + \mathbf{v_p} \times \mathbf{B}\right) \tag{2.18}$$

where $m_p, q_p, \mathbf{v_p}$ are the mass, charge, and velocity of a charged particle, respectively and $\mathbf{B}$ is the magnetic field. Considering the case of zero electric field, the acceleration is:

$$\frac{d\mathbf{v_p}}{dt} = \frac{q_p}{m_p} \left(\mathbf{v_p} \times \mathbf{B}\right),$$

hence the acceleration of the particle is always perpendicular to its direction of motion. This is a centripetal acceleration, and is equal to $v_\perp^2/r$ where r is the radius of gyration. This enables the solution of the radius of the motion [1]:

$$r_L = \frac{m_p v_\perp}{q_p B} \tag{2.19}$$

where r_L is the Larmor radius of the particle and $v_\perp$ is the component of the particle velocity perpendicular to the magnetic field. Particles in plasmas are magnetized if their Larmor radius is shorter than some relevant length scale under study. Given the circular velocity of the particle under consideration and having calculated its Larmor radius, the orbital frequency is [1]:

$$\omega_c = \frac{v_\perp}{r_L} = \frac{q_p B}{m_p}. \tag{2.20}$$

This frequency is known as the cyclotron frequency.

2.3 Hall Thrusters

Like many other electric propulsion devices, Hall thrusters provide impulse to spacecraft by accelerating positively charged ions through an electric field. There are several benefits to this mechanism: First, unlike chemical rockets powered by oxidation reactions the maximum energy available to generate thrust is not limited by the thermodynamic energy available. This allows improvements in propellant velocity and therefore I_{sp}, often by orders of magnitude. Second, the propellant is usually an inert gas with safety benefits over highly reactive, combustible rocket fuels. Third, any means of obtaining electric energy is usable for powering the thruster. However, electric propulsion suffers from the added mass cost of power conditioning for the engine, as well as the much lower thrust available due to power generation limitations. Current design trends in Hall thrusters include development of cylindrical thrusters with no inner channel, concentric configurations with multiple acceleration channels fed by one set of magnetic coils, and notably magnetically shielded designs with the potential to increase the lifetime of Hall thrusters by orders of magnitude [6–10]. These developments notwithstanding, the present research concerns phenomena observed in coaxial Hall thrusters with insulating walls. The following section outlines the operating principles of Hall thrusters as well as relevant physical phenomena in the plasma.

2.3.1 Theory of Operation. Figure 2.2 is a schematic diagram of a coaxial Hall thruster, similar to the ones used in the experiments described here. To operate,

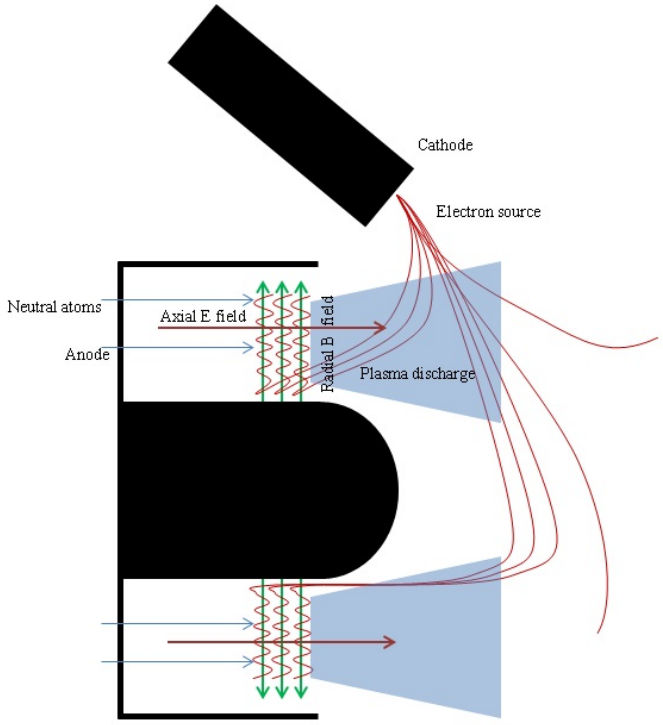

Figure 2.2: Hall thruster diagram.

a positive voltage is applied to the anode with respect to a cathode held at the ground potential. Additionally, either permanent magnets or electromagnets are distributed around the inner and outer channel walls. This creates an axial electric field and a radial magnetic field, with field vectors pointing as shown in Fig. 2.2. Electrons from the external cathode are therefore attracted to the anode. However, the field setup causes the electrons to form a drift current flowing in the $\mathbf{E} \times \mathbf{B}$ direction. This behavior arises directly from Equation 2.18. Considering the steady-state case and crossing both sides by $\mathbf{B}$ we may obtain the electron drift velocity [1]:

$$\mathbf{v_e} = \frac{\mathbf{E} \times \mathbf{B}}{||\mathbf{B}||^2} \tag{2.21}$$

in the case of the Hall thruster, the applied electric and magnetic fields are perpendicular, so the direction of the bulk electron motion is always circular around the channel with magnitude $v_e = E/B$. This closed-drift motion of electrons around the channel is called the Hall current and is the defining characteristic of Hall thrusters, also known as closed-drift thrusters or stationary plasma thrusters due to this phenomenon.

The Hall current thus circulating, neutral atoms injected at the anode enter the region of high electron density and are ionized by electron bombardment and accelerated through the applied potential. Due to their larger mass and the magnetic field strength, the Larmor radius of the ions is longer than the channel length of the thruster. The ions are therefore effectively accelerated only by the axial electric field. Downstream of the thruster channel, electrons from the cathode act to neutralize the plume. The electrons removed during ionization are subsequently trapped in the Hall current and serve to ionize more oncoming neutrals before they eventually drift to the anode and exit the thruster as part of the discharge current.

2.3.2 Efficiency and Loss Mechanisms. The overall efficiency of a Hall thruster is expressed as [1]:

$$\eta = \frac{T^2}{2\dot{m}P_{in}} \tag{2.22}$$

where T is measured thrust, $\dot{m}$ is the total mass flow rate due to the anode and cathode, and P_{in} is the measured total power input to the thruster. This includes the measured discharge power as well as the power required to operate the electromagnets and cathode. A related value is the anode efficiency [11]:

$$\eta_a = \frac{T^2}{2\dot{m}_a I_d V_d} \tag{2.23}$$

where I_d, V_d are the discharge current and voltage, respectively. Equation 2.23 considers the efficiency of only the thruster itself, excluding the magnet and cathode components. These efficiencies are further composed of more detailed terms, not examined here.

The beam power of a Hall thruster represents the amount of power supplied to the system resulting in thrust, neglecting beam divergence. Mathematically, it is:

$$P_b = I_b V_b = n_i q_i v_i A_e V_b \tag{2.24}$$

where I_b, V_b are the beam current and voltage, respectively; n_i is the number density of the ions, q_i is the charge of the ions, v_i is the velocity of the ions, and A_e is the exit area of the thruster. Due to various loss mechanisms, the beam power is always less than the discharge power. These include thermal radiation loss due to heating of the thruster during operation, power loss to the channel walls due to collisions, and loss due to electron collection at the anode. This last term is of concern for the present work.

2.3.3 Anomalous Diffusion. As seen above, some collection of electrons at the anode is unavoidable to preserve quasineutrality of the plasma, and the absolute minimum current to the anode is indeed equal to the beam current [1]. However, experiments using both intrusive and non-intrusive plasma diagnostic techniques show that the electron current to the anode is higher than predicted by classical plasma diffusion theory [6, 9, 12–14]. Various explanations of the phenomenon invoke Bohm diffusion following Janes and Lowder or electron-wall conductivity following Morozov et. al, or some combination of the two [9,12,15]. The definitive cause of the anomalous diffusion is still elusive, as elaborated below.

Anomalous diffusion across magnetic field lines is a broad term applied to many different plasma systems, and connotes the motion of electrons deviating from the "classical" model [4]. Classical diffusion assumes collisional processes between electrons and other species are the sole cause for cross-field transport and results in a diffusion coefficient reminiscent of Fick's law and proportional to $1/B^2$. Contrary to this theory, many systems are found to instead diffuse proportional to $1/B$. This increased diffusion is known as anomalous or Bohm diffusion. In Hall discharges,

the highly fluctuating fields and plasma properties make attribution of anomalous electron transport a difficult task.

Bohm diffusion is usually attributed to instabilities in a plasma system [1]. However, the nature of the instability causing Bohm diffusion in Hall thrusters is still uncertain. Although it was not derived from experiments with Hall thrusters, the theory of Yoshikawa and Rose is frequently invoked [16]. It attributes Bohm diffusion to density fluctuations derived from the magnetohydrodynamic equations for magnetized plasmas. The theory predicts Bohm diffusion will dominate when the mean square deviation of density fluctuations $n(t)$ is much greater than the ratio of collision frequency ν to electron cyclotron frequency ω_e:

$$\frac{\left\langle (n(t) - n_0)^2 \right\rangle_{avg}}{n_0^2} \gg \frac{\nu}{\omega_e}. \tag{2.25}$$

If this condition is not satisfied, classical diffusion is expected. Nonuniform density in the plasma necessarily implies field variations satisfying Gauss's Law as stated in Eq. 2.11, however these remain implicit in the formulation of Yoshikawa and Rose. Another possible explanation for Bohm diffusion given by Janes and Lowder explicitly invokes the electric field caused by an electron density perturbation [12].

The theory of near-wall conductivity developed by Morozov is also proposed to explain the anomalous electron transport in the Hall thruster. It postulates collisions between electrons and the thruster wall as well as reflections from the wall sheath change the azimuthal velocity of electrons. This loss of momentum allows electron drift towards the anode in a very thin layer about the thickness of the electron Larmor radius [15]. This behavior was extensively studied [17–20]; however, there is numerical evidence showing it cannot account for the high electron conductivity observed in experiment [21, 22].

2.4 Hall Thruster Instabilities

Although the plasma flow in an operating Hall thruster appears quiescent to the naked eye, various measurement techniques have revealed many kinds of oscillatory and unstable phenomena in the channel and plume of Hall thruster systems [23]. Existing literature notwithstanding, research interest into instabilities continues due to the effect they have on thruster operation and the general lack of understanding regarding the underlying physical mechanisms of thruster oscillations. This greatly complicates the construction and development of general models of thruster performance to enable better thruster design. The majority of the present research has to do with observing and further characterizing these phenomena, so a general overview is presented here.

2.4.1 Breathing Mode. The best understood mode of oscillation in a Hall thruster is the breathing mode, a large amplitude discharge current oscillation with frequencies in the 1-30 kHz range [11, 23]. High-speed imaging data of the breathing mode shows uniform light emission in the entire channel in cycles corresponding to the current oscillation frequency . First observed by Soviet scientists, the breathing mode was explained theoretically by the one-dimensional numerical two-fluid model of Boeuf and Garrigues [24]. Qualitatively, since electrons in the plasma circulate by design in the Hall current due to the **E** and **B** fields, they quickly ionize neutrals due to their high local velocity and density. The resulting lower neutral density causes the ionization rate to decrease. This leads to a lower number of electrons in the region, since none are supplied by ionization. Neutral flow in that region increases until ionization begins again, restarting the breathing mode cycle. The oscillations numerically found by Boeuf and Garrigues through direct plasma dynamics modeling are also described by the "predator-prey" model of Fife *et. al* which captures similar behavior although it does not reproduce experimental frequencies as accurately [25].

2.4.2 Azimuthal Spokes. A second well-known mode in Hall thruster discharges is the azimuthal spoke mode or ionization instability, first observed by Janes

and Lowder and then by Esipchuk *et. al* [12, 13]. It is defined as a rotating spoke of increased electron density traveling in the $\mathbf{E} \times \mathbf{B}$ direction with cyclic frequencies in the 10-70 kHz range, although some studies have detected azimuthal waves in this frequency regime moving in the opposite direction [26]. The frequencies are associated with the group velocity of the spoke around the channel, and signal analysis has revealed higher modes of oscillation within these spokes [27]. Janes and Lowder observed spokes traveling with approximately 1/5 the predicted Hall current velocity [12]. In high-speed imagery, bright spokes rotating in a similar manner are documented in both coaxial and cylindrical Hall thrusters [7, 28, 29].

Spokes were immediately theorized to contribute to the anomalous electron transport discussed above. This connection was due to the observation of an azimuthally varying electric field associated with the motion of the spoke. Janes and Lowder demonstrated theoretically how this would allow electrons to move across the $\mathbf{B}$ field lines, and the calculated current was found to agree with the predictions of Yoshikawa and Rose [12]. Thus, azimuthal spokes in a Hall thruster discharge may contribute to Bohm diffusion. More recent studies performed on the discharge current of Hall thrusters with segmented anodes have corroborated the association of spoke passage with increased discharge current on those segments [6, 9].

Recent efforts have focused on developing a numerical model capable of explaining the source of azimuthal waves using both two- and three-dimensional models. These have succeeded in reproducing some of the electron diffusion observed in experiments [8, 30–32]. However, the underlying cause of these instabilities is still unknown. Lam, using a 2-D hybrid fluid/Particle-In Cell (PIC) model, proposes that the instabilities arise when plasma density fluctuations correlate with velocity fluctuations [32]. This provides a possible causal chain from incipient plasma fluctuations to electron transport to the anode. Concurrent measurement of plasma density and velocity is necessary to corroborate these findings by experiment.

2.4.3 Other Oscillations. Oscillations at higher frequencies extending into the RF range are also observed and theorized to contribute to thruster performance [23,27]. However, the amplitude of these phenomena are smaller than those described above and generally require even more specialized equipment than is typical due to their extremely high frequency.

2.5 Measurement Techniques

Many instruments are used to measure the local properties of plasmas. The following provides a description of two types, the emissive probe and the Hall current sensor. Emissive probes have a long heritage dating to Langmuir and are relevant in many plasma applications, while the Hall current sensor is a new development designed especially for use with Hall thrusters [33,34]. The third measurement technique used in the present research, high-speed imaging, is not based on plasma dynamics and so is detailed in the next chapter, as are the explicit descriptions of the other instruments used.

2.5.1 Emissive Probe Operation. Plasmas carrying electric fields also carry potentials and thus localized charge distributions. Therefore, the local potential in a plasma is a useful value for determining electron and ion populations and motion. In addition to collecting probes such as Langmuir probes, probes emitting electrons into plasma provide useful information about local plasma properties [9,33]. The emissive probe is especially suited to Hall thrusters, since it is effective at measuring potentials in streams of moving plasma, unlike collecting probes [35]. Although there are several techniques for measuring plasma potential with emissive probes, only two are covered here.

When a wire biased below the plasma potential is placed in a plasma, a positive sheath develops around it as described above and a current flows into the probe. If the wire or filament is made of a suitable material, it emits electrons thermionically when heated. In this case, when the bias potential of the probe passes through the

plasma potential, the net current to the probe will be zero. Figure 2.3 shows the notional current-voltage trace of an emissive probe sweep. This method assumes the

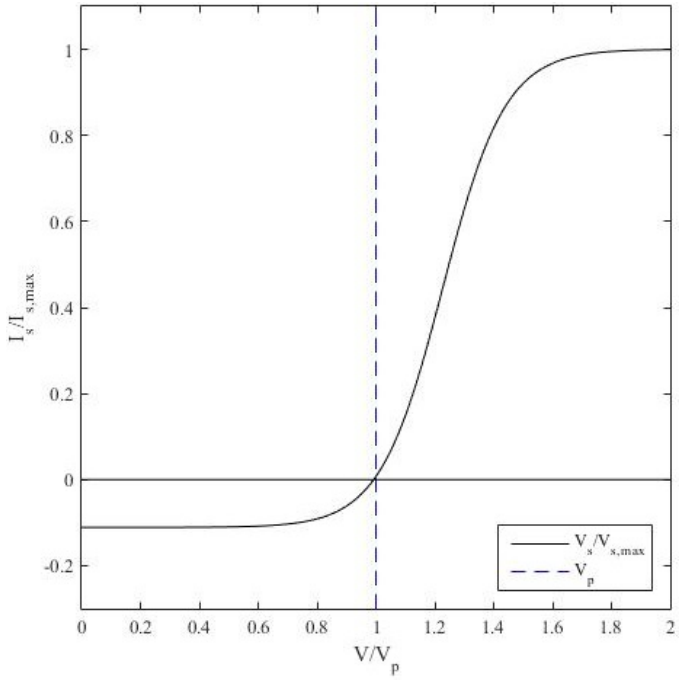

Figure 2.3: Notional emissive probe I-V characteristic.

thermionic emission of electrons occurs with zero energy, equivalent to neglecting the effect of space charge. For the planar case, the potential V actually approaches T_e/e^-, the ratio of electron temperature to charge [36]. For many applications this is an adequate measurement, particularly when speed is unimportant. However, this method is poorly suited to time-resolved measurements at high sampling rates due to the need to conduct a voltage sweep.

The method used in the present research was developed by Kemp and Sellen in 1966 and is based on allowing the emissive probe potential to vary freely relative to the laboratory ground, or float, through the use of a large load resistor [33]. The current in this load resistor is then used to determine the potential drop at the center of the probe filament. In this case, the floating potential of the probe V_f is [37]:

$$V_f = V_p - T_e \ln\left(\frac{I_{s,e}}{I_{s,i} + I_{e,e}}\right) \tag{2.26}$$

where V_p is the plasma potential and $I_{s,e}, I_{s,i}, I_{e,e}$ are the electron saturation current, ion saturation current, and electron emission current, respectively. The measured V_f tends towards the plasma potential as $I_{e,e}$ is increased, providing a good estimate as long as $\ln\left(I_{s,e}/\left(I_{s,i}+I_{e,e}\right)\right) > 1$, as is shown in Fig. 2.4. In particular, V_f is a good

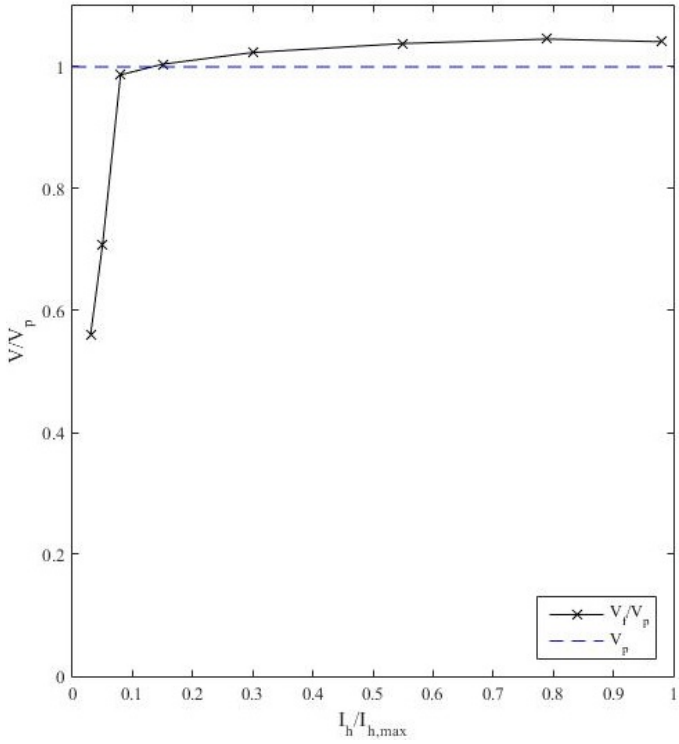

Figure 2.4: Emissive probe floating potential characteristic [33].

surrogate for V_p if the quantity under examination is a relative change in V_p rather than V_p itself. The frequency response of the floating potential measurement extends into the low RF range allowing time resolved plasma potential measurements at high sampling rates [33].

2.5.2 Hall Current Sensor Operation. In the steady case, the Biot-Savart law describes the magnetic field at a location $\mathbf{B}(\mathbf{r})$ due to a current distribution at some other location $\mathbf{J}(\mathbf{r}')$:

$$\mathbf{B}(\mathbf{r}) = \frac{\mu_0}{4\pi}\oint_{Q'} \frac{\mathbf{J}(\mathbf{r}')\times(\mathbf{r}-\mathbf{r}')}{||\mathbf{r}-\mathbf{r}'||^2}\, dQ' \tag{2.27}$$

where μ_0 is the permeability of free space and Q' is the volume containing all current elements [5]. The Biot-Savart law thus provides a means of solving the classic (direct) magnetostatics problem: given some current $\mathbf{J}$ localized at some region in space, determine the magnetic field $\mathbf{B}$ at some arbitrary location induced by it. More relevant for the present research is the inverse problem: given $\mathbf{B}$ at some set of locations, determine the current density $\mathbf{j}$ at a different location. The following outlines the solution method developed by Rubin and implemented by Mullins for the purpose of Hall thruster diagnostics [34, 38, 39].

2.5.2.1 Direct Problem for Fixed Geometry. Figure 2.5 shows the setup of the direct problem in the planar case. The solution space for the current

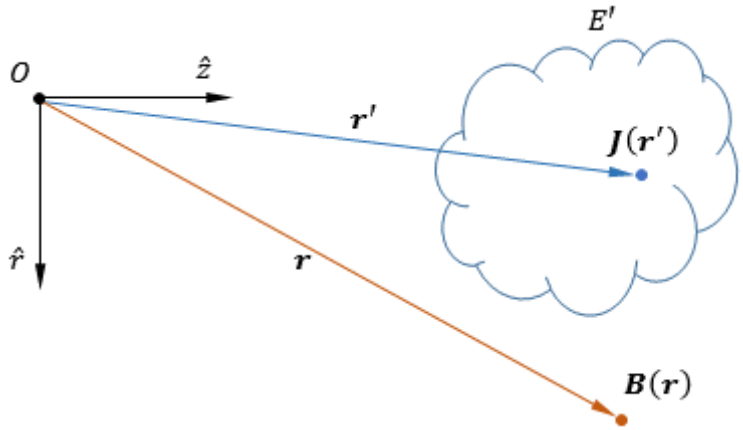

Figure 2.5: Current solution geometry.

is a surface inside the Hall thruster channel coplanar with the magnetic sensor, *i.e.* in the r-z plane. This assumes all current measurable by the magnetic sensors is steady, axisymmetric, and intersects the plane. Additionally, the magnetic field in the azimuthal direction is not measured due to sensor construction. Finally, a material with some unknown permeability μ is assumed. Under these conditions, Equation 2.27 reduces to:

$$B_r(\mathbf{r})\hat{\mathbf{e}}_\mathbf{r} + B_z(\mathbf{r})\hat{\mathbf{e}}_\mathbf{z} = \frac{\mu}{4\pi}\oint_{E'} \frac{-J_\theta(\mathbf{r}')(z-z')\hat{\mathbf{e}}_\mathbf{r} + J_\theta(\mathbf{r}')(r-r')\hat{\mathbf{e}}_\mathbf{z}}{(r-r')^2+(z-z')^2}\, dr'dz' \qquad (2.28)$$

where $\hat{\mathbf{e}}$ indicates a unit vector in the subscripted direction and E' is the area of integration. Next, assume that the total area of integration is divisible into n areas of piecewise constant current density, so each may pass outside the integral and Eq. 2.28 becomes:

$$\begin{aligned} B_r(\mathbf{r}) &= \sum_{i=1}^{n} \frac{\mu J_{\theta,i}}{4\pi} \oint_{E_i'} \frac{-(z-z')}{(r-r')^2+(z-z')^2}\, dr'dz' \\ B_z(\mathbf{r}) &= \sum_{i=1}^{n} \frac{\mu J_{\theta,i}}{4\pi} \oint_{E_i'} \frac{(r-r')}{(r-r')^2+(z-z')^2}\, dr'dz' \end{aligned} \tag{2.29}$$

where i is an index indicating the area and the current element under examination. Now in each case the integral depends only on the position of the magnetic sensor $\mathbf{r}$ and the area E_i, so each of these integrals is a constant based on geometry. Additionally, each sensor measures only in one direction, so only one of Eqs. 2.29 will apply in any case. So for a given sensor field value B_j:

$$B_j = \sum_{i=1}^{n} A_{ij} J_i \tag{2.30}$$

where A_{ij} is a constant coefficient depending on the permeability of the space between the current density element and the sensor as well as the size of E_i and the relative location of the sensor and current element and we have eliminated the extraneous subscript on the current. Finally, the matrix relation for each current element to all sensors is obtained:

$$A\mathbf{J} = \mathbf{B} \tag{2.31}$$

where A is the Green's matrix of constant coefficients relating $\mathbf{J}$, the column vector of currents at area elements, to $\mathbf{B}$, the column vector of magnetic sensor values. Also note the background magnetic field from the Hall thruster coils was not considered in this derivation, but this contribution to the measured $\mathbf{B}$ is assumed constant whether the plasma discharge is running or not, and subtracted from $\mathbf{B}$ by the principle of superposition after measurement with the thruster off but the coils on [34, 38, 39].

2.5.2.2 Inverse Problem. Equation 2.31 formulates the direct magnetostatic problem for the sensor as designed. The solution of the inverse problem is still extremely underdetermined and poorly conditioned: In the research presented here solution of 80 values in the **J** vector is attempted using measurements from only 8 magnetic sensor locations. A first attempt is to solve the inverse problem via the linear least-squares method, the set of values **J** satisfying

$$\text{Min}||A\mathbf{J} - \mathbf{B}||. \tag{2.32}$$

This least squares solution, however, does not produce meaningful physical solutions so a matrix regularization is used to incorporate information about the problem known *a priori*. This is achieved via Tikhonov's method, which finds **J** by minimization:

$$\text{Min}\left[||A\mathbf{J} - \mathbf{B}||^2 + \lambda^2||L\mathbf{J}||^2\right] \tag{2.33}$$

where L is the Tikhonov regularization operator and λ is the regularization parameter chosen in each case via a method described below. For this problem the best regularization operator is:

$$L = \frac{\partial^2}{\partial r^2} + \frac{\partial^2}{\partial z^2} + 2\frac{\partial^2}{\partial r \partial z} \tag{2.34}$$

corresponding to enforcing smoothness on the solution. Additionally, solutions for the current are constrained to be non-negative and zero boundary conditions are enforced both against the wall and at the upstream and downstream limits of the solution space [39].

2.5.2.3 Calibration. With the solution method in hand, it remains to determine the Green's matrix A. This is accomplished via the use of a set of calibration coils inserted into the Hall thruster channel. A known current is passed through each wire loop in the coil located at a known position in the channel. Then

the magnetic field due to the current is observed with the Hall thruster magnetic field on at operational conditions. This process is repeated for each of the 80 calibration locations in the channel, making a solution grid with 8x10 cells. The A matrix is thus the 80×8 matrix of values A_{ij} in Equation 2.30.

2.5.2.4 Choice of Regularization Parameter. Solutions to the minimization problem 2.33 are calculated for a range of λ values. Then, the solution minimizing the value $\ln ||A\mathbf{J} - \mathbf{B}||^2 + \ln ||L\mathbf{J}||^2$ is chosen. This corresponds to the optimal value. In the case of time-resolved data, calculation of the optimal λ for each timestep is extremely computationally intensive. Finding λ at one timestep and using it for each point in time in a dataset is a reasonable alternative and does not degrade the solution [34].

2.5.2.5 Comments on Constraints. The constraints enforced on the solutions for current are recognized as not entirely physical. Specifically, driving current to zero at the upstream and downstream solution boundaries presumes *a priori* knowledge of the location of current phenomena. Additionally, zero boundary conditions at the wall are probably inaccurate; although the walls of Hall thrusters are insulating, electron-wall collisions including absorption are a known erosion mechanism and represent a current at the walls [1]. Finally, any structures such as near-wall conductivity will occur below the resolution limit of the solution. In spite of these limitations, the analysis techniques described above are the state-of-the-art and are useful for capturing many effects including the breathing mode [34].

2.6 Motivation

Although none of the data collection methods or plasma phenomena under study are novel, the high-frequency, synchronized measurement of several properties of the plasma discharge in a Hall thruster provides insight into the structure of the plasma during oscillations. Resolving the plasma potential, Hall current, and luminous emission of the channel in time during a single thruster phenomenon allows the develop-

ment of possible causes and mechanisms for oscillations in the plasma both supporting the previous research and allowing new development of the physical basis for phenomena in the flow. The present research aims to provide such synchronized data.

III. Experimental Setup and Methodology

3.1 Laboratory

For this research, experiments were carried out in the Space Propulsion Application Simulation System (SPASS) Laboratory at the Air Force Institute of Technology (AFIT), Wright-Patterson AFB, Ohio. The SPASS lab vacuum chamber is approximately cylindrical with a length of 2.5 m and a 0.9 m radius, equating to an approximate total volume of 6.4 cubic meters. An Oerlikon/Leybold Vacuum Screwline SP 250 roughing pump performs the first stage of chamber evacuation, followed by four CVI Torr Master® 20 inch TM500 helium cooled cryopumps. Combined with a final helium cooled cryo plate assembly mounted on the chamber ceiling downstream of the thruster, the pumps have a 21,000 L/s pumping capacity to maintain pressures less than or equal to 3×10^{-7} torr with no gas flow into the chamber, or approximately 3×10^{-5} torr with a thruster operating. Chamber pressure was measured during operation with an ExTorr Residual Gas Analyzer.

Seven ports around the chamber allow for the mounting of 25 cm diameter quartz windows to enable visual inspection of thruster operation as well as high-speed image data collection. During thruster operation, sputtering erosion of surfaces exposed to the ion plume can cause a thin layer of material to build up on the ports, slowly degrading their ability to transmit optically and necessitating periodic removal and polishing. This occurs on the timescale of hours of thruster operation and was not found to affect measurement of relative brightness during data collection in the present research.

Inside the chamber, the thrusters were mounted to a three-axis movement stage held fixed during data collection. Gas supply was metered through two MKS flow controllers from a supply of 99.9995% pure propulsion grade xenon. Downstream of the thrusters, large sheets of graphite foil were mounted to serve as sacrificial material to reduce sputter erosion of the chamber. Electrical feedthroughs allowed the placement of power supply for the thrusters as well as all electronic sensing components outside the chamber. A water cooling system in the chamber allowed equipment exposed to

the thruster plume or other heating loads to maintain a stable operating temperature throughout the experiments.

3.2 Thruster Setup and Test Method

Breathing and spoke modes in a commercially available 600 W thruster were examined. Additionally, limited tests were conducted with a smaller 200 W thruster to determine the feasibility of extending the sensor setup to other thrusters. An electride cathode was used in lieu of the hollow cathode supplied by the thruster vendor. This substitution led to a cathode mass flow rate approximately 20% of the anode mass flow in order to achieve stable cathode operation. In the present experiments, the applied current to the magnetic coils of each thruster was held constant, while discharge potential, V_d, and anode mass flow rate, $\dot{m}_a$, were varied as required. Breathing mode data was obtained by running the thruster at full power within 10% of the manufacturer recommended discharge potential and anode mass flow rate. In these conditions, azimuthal features were suppressed. Spoke mode data was obtained by lowering V_d up to 50% and increasing $\dot{m}_a$ around 10% from the nominal values in an effort to promote density instabilities. This led to stable overall thruster operation at a higher discharge current I_d while exciting azimuthal oscillations. Figure 3.1 shows a schematic and actual image of the experimental setup. Note in Fig. 3.1(b) the bright patch produced by the emissive probe. The feature was removed in analysis to improve visual identification of spoke modes when false color was applied.

Thruster power was supplied through a power processing unit (PPU) mounted outside the chamber. Anode and cathode gas flow was metered through MKS flow controllers. During thruster operation, a flow oscillation with a period of approximately 30 s was sometimes observed in the cathode line. The gas supply line setup was identified as a potential cause, and the oscillation was not under examination during the experiments. Due to its long period, the flow oscillation was not observed to contribute to experimental phenomena under study.

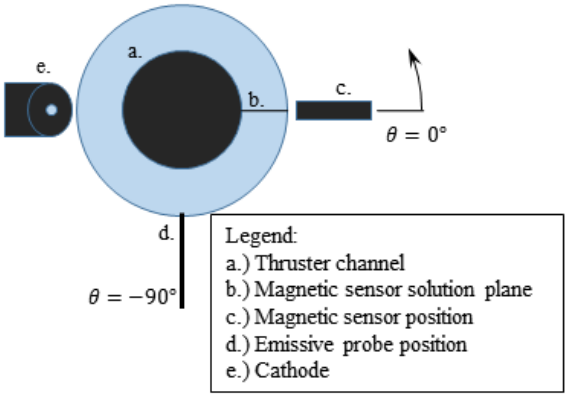

(a) Thruster Instrumentation Schematic

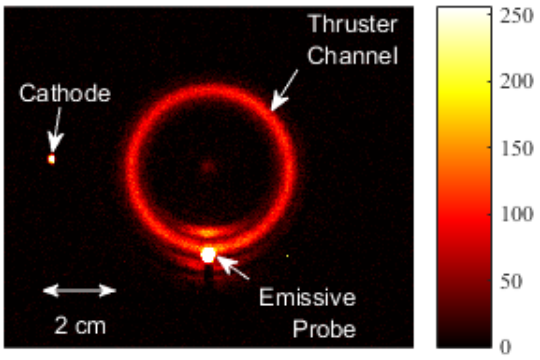

(b) Example image of thruster direct emission. False color, 750 ns exposure time, arbitrary intensity, annotations added.

Figure 3.1: Experimental configuration.

Figure 3.2 shows the signal flow for data collection. Any given data collection run began with a 5 V transistor-transistor logic (TTL) pulse from the oscilloscope near-simultaneously activating acquisition from the high-speed camera, magnetic sensor DAQ, and emissive probe DAQ.

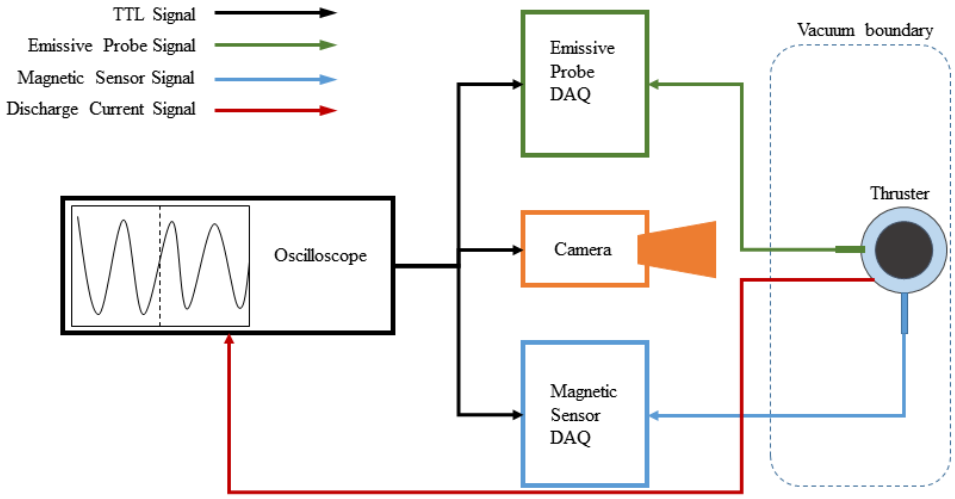

Figure 3.2: Signal flow in experiments.

In addition to raw data from the three sensors, the output discharge current waveform from the oscilloscope was recorded, as well as timing data from the magnetic sensor DAQ and sometimes the high-speed camera. Data collection and analysis is further detailed below.

3.3 High-Speed Imaging

A Shimadzu Hyper Vision HPV-2 high-speed video camera was used to capture video of thruster operation. The camera setup as used for testing is shown in Fig. 3.3. In each recording, the HPV-2 captures 102 frames of 312 × 260 pixel images at rates up to 1 million frames per second (Mfps). The complementary metal-oxide

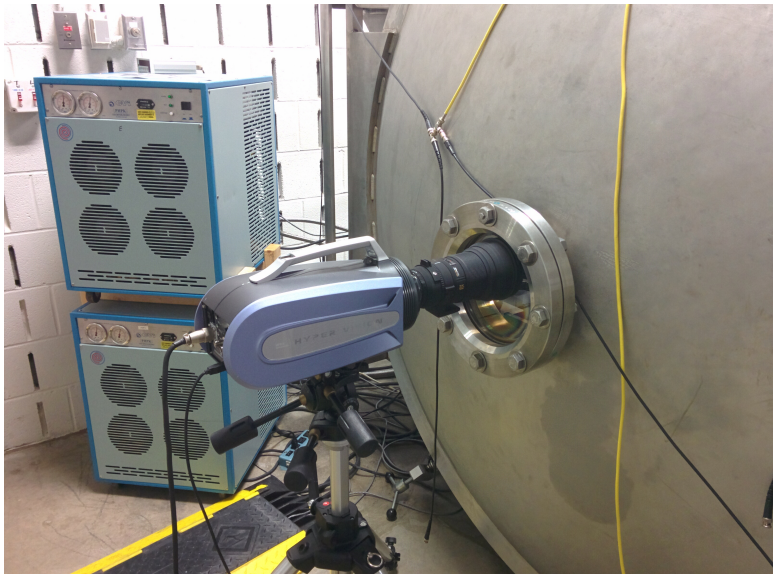

Figure 3.3: Camera setup.

semiconductor (CMOS) sensor is sensitive to radiation across the visible spectrum, so resulting images are panchromatic. All images containing high-speed camera data presented herein are of arbitrary intensity and have false color applied, as shown by the colorbar accompanying each image. Images of each thruster were obtained at a 750 ns exposure time through a 300 mm Nikon lens with an f-stop of 2.4 to maximize the light incident on the CMOS sensor. Since the Hall thrusters are emitters, no

additional lighting was used. However, it was necessary to use the HPV-2's digital gain control at factors of 10-30x to obtain images usable for visual analysis.

In order to correlate the high-speed video data with the other experimental sensors, the HPV-2's external triggering function was used. When the trigger is received the camera is able to synchronize its output to an image buffer to within 1 µs for images taken at 1 Mfps. Figure 3.4 represents the triggering operation of the camera schematically. Note that the first frame of the video is always the frame the

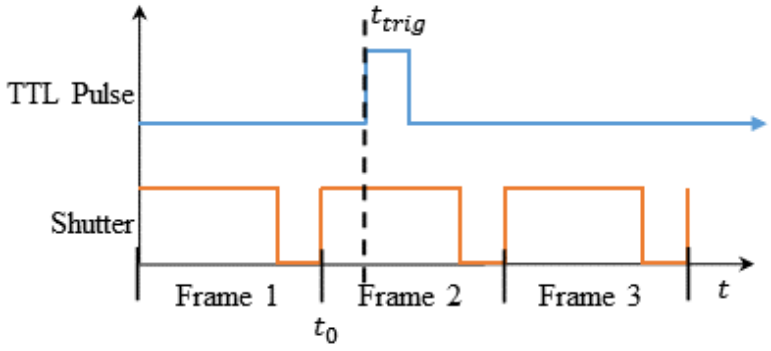

Figure 3.4: Camera triggering schematic. t_0 indicates the start time of a video, t_{trig} indicates the true time of trigger arrival.

trigger arrived, regardless of where in the 1 µs frame the pulse was actually detected. This implies the time uncertainty associated with each frame time t_{frame} is t_{frame} + 1 µs. Note that the uncertainty is asymmetric, *i.e.* events may occur later than frame time but not measurably earlier.

Image analysis was conducted with Matlab®. To visualize the videos as still images and to enable easier analysis, the circular thruster channel was projected onto a vertical line centered at the $\theta = 0°$ or 3 o'clock position in a technique similar to Sekerak [9]. Figure 3.5 illustrates this process. In the image analysis, 180 blocks were used instead of the four shown in the schematic of Fig. 3.5, mapping each vertical pixel of the resulting image to the average brightness of a 2° band of the thruster channel. Next, the projected channel of each frame in a video was aligned horizontally to show the progression in time of the channel brightness. False color was used to allow visual examination of data and observation of plasma emission structures in the

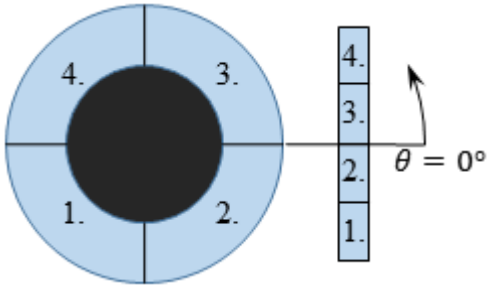

Figure 3.5: Schematic demonstration of channel projection.

thruster. Figure 3.6(a) shows an example projected-channel plot of the thruster in a globally oscillating breathing mode, so the plot shows uniformly varying columns as the thruster channel flashes on and off. Figure 3.6(b) shows the thruster exhibiting the spoke mode, and diagonal features pointing from the lower-left side of the plot to the upper-right side indicate spokes propagating in the counterclockwise direction. Another advantage to these plots is the relative ease of determining the velocities

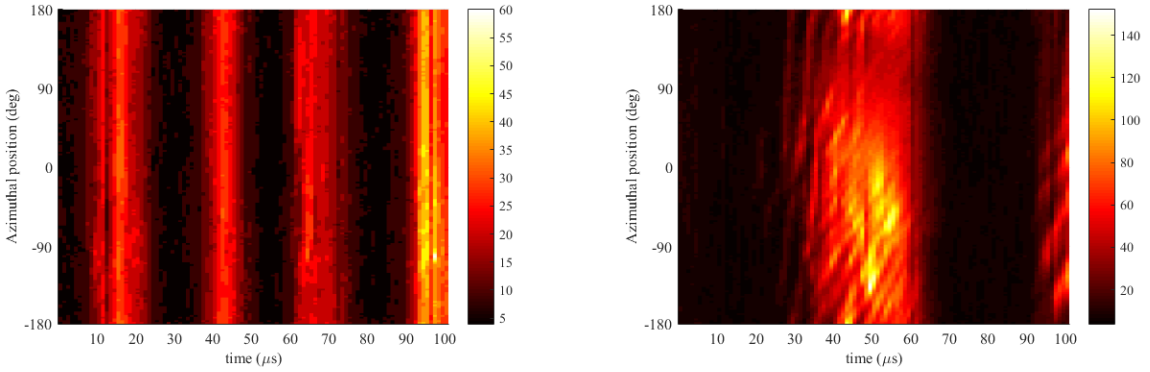

(a) Thruster exhibiting breathing mode

(b) Thruster exhibiting azimuthal spokes

Figure 3.6: Example projected-channel video plots

of spokes as they propagate around the thruster face. Since time is on the x-axis and azimuthal position is on the y-axis, the slope of any spoke is its propagation velocity. The slope may be measured directly or by translating the columns of a projected channel plot by a fixed multiple of their location within the image until the spoke under examination appears horizontal. In this case, the number of pixels

shifted provides the distance traveled in a frame. Expressed as the periodic frequency of a spoke completing a cycle around the channel with equivalent speed, the velocities of the spokes on the lower half of the thruster from 40 to 60 µs in Fig. 3.6(b) range from 17-22 kHz. Note: this frequency is not the same as the one observed on a Fourier transform of any given azimuthal location, as any such transform observes the passage of spokes in groups or clusters as seen in Fig. 3.6(b).

As a final note on image analysis, emission from plasma in the axial range of the solution space of the magnetic sensor was assumed much greater than emission outside the domain, with the exceptions of the "central spike" of the plume and the cathode discharge. In other words, it was assumed the features observed in the images were of plasma structures in the region detectable by the Hall current sensor.

3.4 Magnetic Sensor

Measurements of magnetic field fluctuations around the thruster were performed with a sensor probe developed and constructed by Plasma Controls to measure the Hall current in Hall thrusters. The probe uses an 8-sensor planar array of 8 Micro-Magnetics STJ-240 tunneling magnetoresistance (TMR) sensors, with four each in the thruster radial and axial directions. In order to obtain data sufficiently above the noise floor of the outermost TMR sensors, it was necessary to position the probe slightly impinging in the plume of the thruster. To protect the sensors from the plasma environment, they are covered by a graphite-coated stainless steel housing to reduce sputtering. The probe was connected to the water-cooling system in the chamber to maintain suitable operating temperatures for each sensor. A Li-ion battery was used to supply a constant voltage to the sensor array. Figure 3.7 shows the magnetic sensor in its housing. Sensor output of all 8 channels was acquired simultaneously by an NI USB-6366 Data Acquisition system (DAQ) at a rate of 2 million samples per second (2 MS/s). the DAQ was triggered via the same TTL pulse used to trigger the HPV-2. Latency of the trigger was determined by the delay between the rising edge of the DAQ pulse indicating sample acquisition and the arrival time of the rising

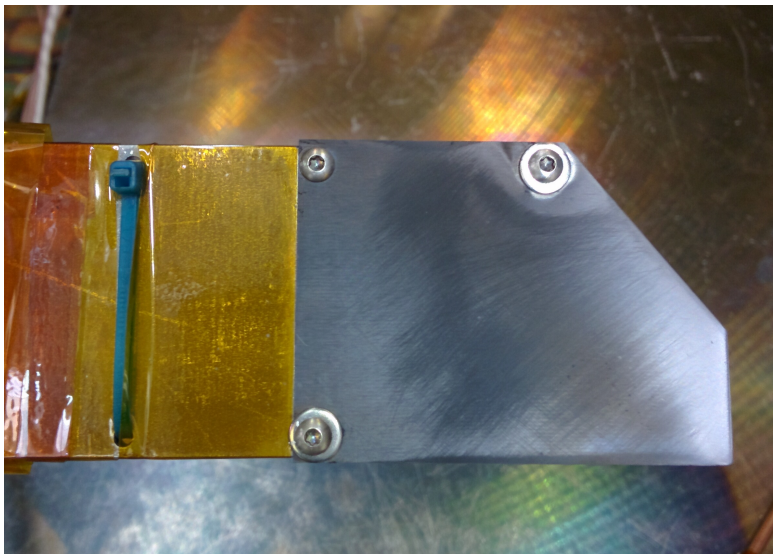

Figure 3.7: Photograph of magnetic sensor assembly.

edge of the trigger pulse. Typical delays observed in experiment were 0.1 µs with a maximum observed delay of 0.11 µs.

Sensor calibration was performed with a set of circular coils. Plastic spacers were used to position the coil in the thruster channel at the appropriate location. Next, a current was run through each coil in sequence while the magnetic field was read by each sensor. The relation between the known current at each location and the measured value at each sensor is the value of the Green's matrix as described in Eq. 2.30. The zero current at any other location in the solution space during calibration allow isolation of each value of the Green's matrix A.

3.4.1 Post-processing. Data from the NI USB-6366 was processed in Matlab® using algorithms implementing the solution method described in Chapter II. The raw 2 MS/s data was downsampled with a four point moving average to 250 kS/s in order to reduce high-frequency noise as shown in Eq. 3.1:

$$\bar{b}_{i'} = \frac{1}{4} \sum_{i=4(i'-1)}^{4i'-1} b_i \tag{3.1}$$

where $\bar{b}_{i'}$ is the downsampled value at index i' and b_i is the raw value at index i. This low-pass filtering introduced a quantifiable timeshift to the data; for a set of raw samples taken at times t_i, the corresponding downsampled time $\bar{t}_{i'}$ is their average:

$$\bar{t}_{i'} = \frac{1}{4} \sum_{i=4(i'-1)}^{4i'-1} t_i = t_{4(i'-1)} + 0.75\,\mu\text{s} \tag{3.2}$$

where the timeshift due to downsampling is 0.75 µs as shown.

After analysis, a 2-D map of current density in the solution space of the Matlab® algorithm was obtained. In order to cross-correlate visible emission data with magnetic sensor data, the total current through the solution plane was found as a function of time by summing the current densities in each element of the solution space. Through synchronization, the total current through the solution plane at $\theta = 0°$ is directly comparable to the visible emission from the same location.

3.4.2 Magnetic Probe Error Sources. Obtaining spoke data from the magnetic sensor was more difficult than the same task with the emissive probe. First, comparatively few spokes were observed passing by the magnetic sensor. Second, the magnetic sensor's effective sample rate masked any current features with frequency greater than 1 MHz during its noise filtering process. Third, to obtain Hall current data from the magnetic sensor, the minimization problem Eq. 2.33 was solved based on the assumption of steady, smooth currents like the breathing mode rather than the unsteady currents associated with the azimuthal mode. The solution method was also sensitive to an accurate calibration dataset. Fourth, the magnetic data carries a time uncertainty of ±0.25 µs over and above the 1 µs uncertainty in the video data. This makes determination of actual thruster behavior difficult at the desired timescale. Finally, the 600 W thruster used is lower powered than the thruster the magnetic sensor was designed to work with [34]. This means the Hall current generated by the thruster is weaker and thus more difficult to measure with the magnetic sensor.

3.5 Emissive Probe

The emissive probes used for the current experiments were also developed by Plasma Controls. The probe consisted of a 0.13 mm diameter wire loop protruding from double-bore alumina tubes as shown in Fig. 3.8. The emissive probe was heated

Figure 3.8: Emissive probe detail. Ballpoint pen for scale.

by a 3.65 V potential from a battery floating with the probe, while the floating potential was sampled across a resistor divider at 62.5 MS/s by a PicoScope as shown in Fig. 3.9. The probe was positioned within the axial range of the Hall current solution space, so the emission perturbed the plasma. Data acquisition was triggered by the same TTL pulse used for the other sensors and was referenced to a buffer in a manner similar to the HPV-2. The higher sample rate provided by the PicoScope implies that the time uncertainty of emissive probe measurements is 8 ns.

3.5.1 Procedure for Comparison with Video Data. Comparison of emissive probe potential data with visible emission of the thruster plasma was complicated

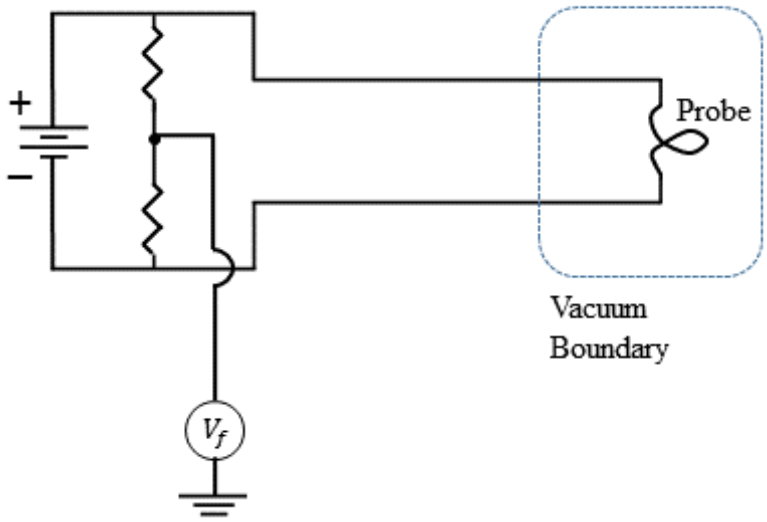

Figure 3.9: Emissive probe circuit diagram.

by the brightness of the emissive probe. As seen in Fig. 3.1(b), the probe occludes the thruster channel and prevents direct observation of the $\theta = -90°$ location of the channel. Due to this phenomenon, video data from the unaffected $\theta = -80°$ location of the channel was used for comparison to plasma potential data instead. For global phenomena such as the breathing mode, this substitution caused no observable effect since the entire channel was emitting uniformly. However, local phenomena presented an additional analysis challenge. Figure 3.10 shows an example of spokes passing the emissive probe on a projected-channel plot. Note the noisy and dark data in the $\theta = -90°$ location of the plot due to removal of light emitted by the emissive probe. Data from the $\theta = -80°$ position is not directly usable to describe phenomena at the emissive probe location since spokes rotate azimuthally by definition. To compensate, the spoke structure was assumed not to evolve in the time it took to travel between the probe location and $\theta = -80°$. Then, the video data from the $\theta = -80°$ was shifted backwards by a time $t_{shift} = 10°/\dot{\theta}_{spoke}$, where $\dot{\theta}_{spoke}$ is the spoke velocity in degrees per second, to compensate for the spoke's travel. This process is illustrated schematically in Fig. 3.11. This process was repeated for spokes of different velocities as necessary, sometimes within the same video. Unless otherwise noted, comparison

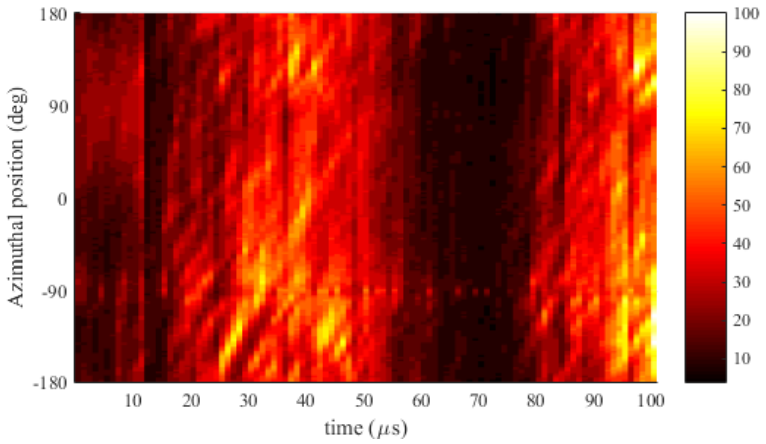

Figure 3.10: Example of spoke passage occluded by emissive probe.

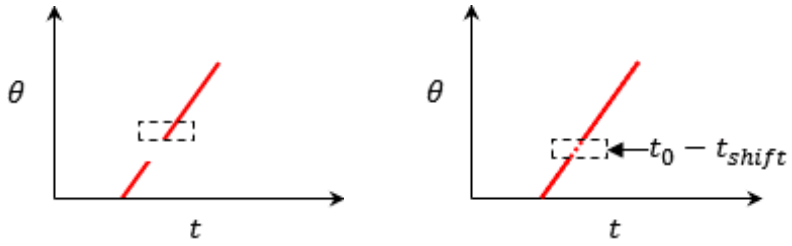

(a) The red spoke has a gap due to the emissive probe. Data from the dashed-line box is substituted to compensate.

(b) the video data from the box was timeshifted and substituted for the missing data.

Figure 3.11: Description of data substitution for spoke analysis.

of emissive probe and visual data during the spoke mode was timeshifted according to this method.

3.5.2 Variation: Use as cold probe. Limited tests were conducted with cold Langmuir probes to examine the feasibility of measuring plasma potential fluctuations without using an emitting probe, using only supplies on hand. One side of a used emissive probe was repurposed as a cold probe, and the current through the probe when exposed to plasma was measured as the potential drop across a resistor as shown in Fig. 3.12. In this case, the current through the probe ought to vary as the plasma potential since ground is fixed. The current is obtainable from V_1 by using Ohm's law.

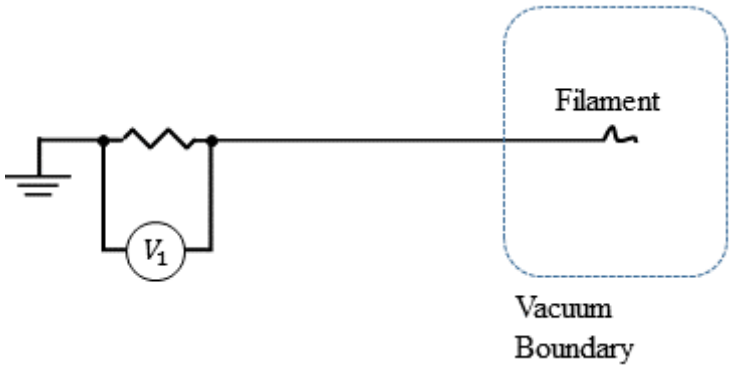

Figure 3.12: Cold probe circuit diagram.

3.5.3 Emissive Probe Error Sources. Several sources of emissive probe timing error may exist. First, misalignment of the probe's angular position on the thruster face would introduce a uniform bias, as the probe was not moved between tests. Second, the spoke velocity calculation method was based on shifting pixels in the projected channel plots. The requirement to shift an integer number of pixels grouped the spoke velocity into 2 deg/µs bins, although some estimation of intermediate velocities was attempted. Due to the high angular resolution of projected channel plots and camera framerate, velocity errors of this type introduce timing errors of less than 1 µs. Since several spokes were observed in each velocity bin, the cumulative effect is to reduce the resolution of measurement rather than to introduce systemic bias. Finally, the 1 µs timing uncertainty of the camera means features occurring within 1 µs of any given frame time are not resolvable. However, it is reasonable to assume the distribution of trigger points within the initial frame are distributed randomly across many test runs. Therefore, it is reasonable to observe trends applying to the entire dataset.

There is certainly error in directly associating plasma potential with the floating potential of an emissive probe, as stated in Eq. 2.26. However, the second term in Eq. 2.26 varies slowly for emissive probes. Therefore, associating changes in the normalized plasma potential with changes in the normalized floating potential is well-founded and errors are much smaller than the features under examination.

3.6 Summary

The experimental setup as detailed above provided the following data products: a video subsequently converted to a projected-channel plot, a time series of emissive probe floating potential readings, and a time series of current density distributions in the solution space. Additionally, the discharge current waveform used to trigger each test run was recorded from the oscilloscope. Comparison of the data from each sensor type allows examination of plasma structures as they evolve in time. In the case of azimuthally varying phenomena, it is possible to infer limited information about the spatial structure of the plasma, as seen in Chapter IV.

IV. Results

4.1 Global Oscillations: Data

Three tests were performed to characterize the thruster breathing mode. Figure 4.1 shows the projected-channel plot of breathing mode test 1. Figure 4.2 shows the normalized video intensity at $\theta = 0°$ compared with the normalized Hall current solution from the magnetic sensor.

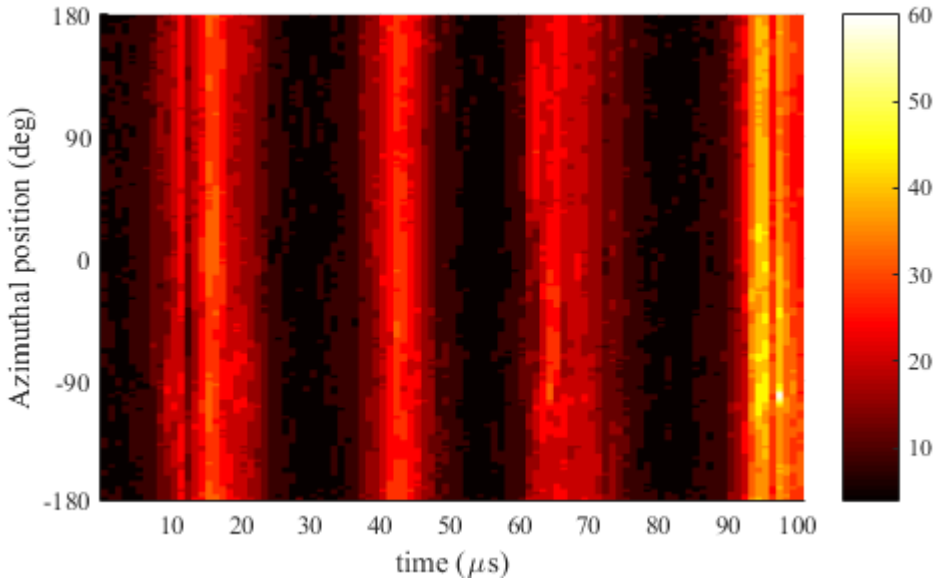

Figure 4.1: Breathing mode test 1 projected channel plot. Arbitrary intensity.

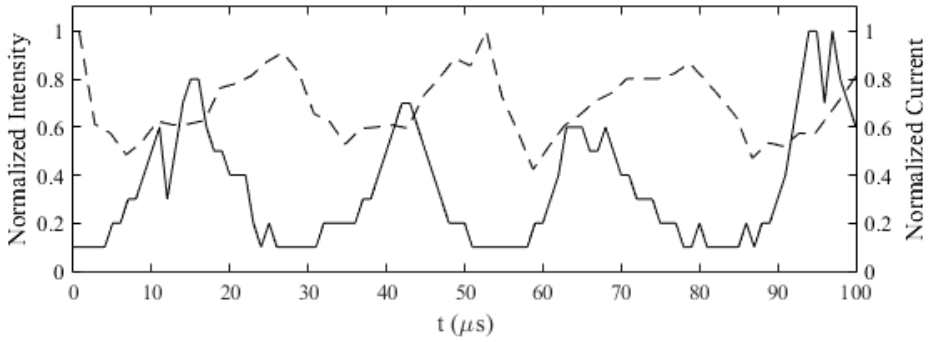

Figure 4.2: Breathing mode test 1 magnetic and video data comparison. Solid line: video data. Dotted line: magnetic data.

In Fig. 4.2 the direct emission intensity attained local maxima at $t = 15.5, 42.5, 64,$ and 94.5 µs. The Hall current solution attained local maxima at $t = 26.75, 52.75,$ and

78.75 µs. The average delay between a video maximum and a Hall current maximum was 12.08 µs. Fourier analysis of both datasets shows a breathing mode frequency of 39 kHz.

Figure 4.3 shows the projected channel plot of breathing mode test 2. Note the breathing mode was disrupted at $t = 70$ µs by an unknown cause, possibly related to the onset of a cathode flow fluctuation during the data collection period. Figure 4.4 shows the normalized video intensity at $\theta = 0°$ compared with the normalized Hall current solution from the magnetic sensor for breathing mode test 2. In this case,

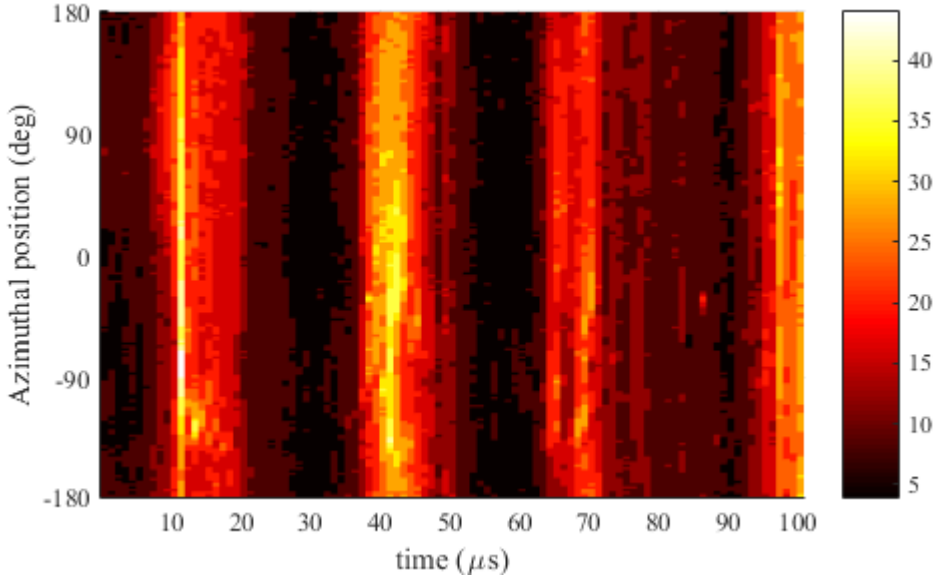

Figure 4.3: Breathing mode test 2 projected channel plot. Arbitrary intensity.

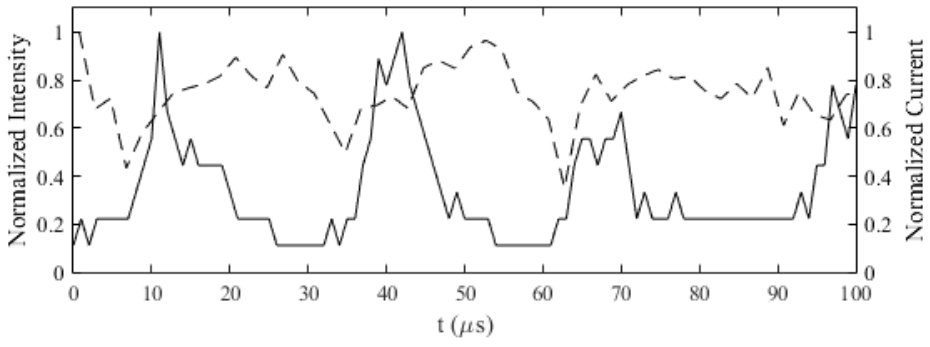

Figure 4.4: Breathing mode test 2 magnetic and video data comparison. Solid line: video data. Dotted line: magnetic data.

local maxima in direct emission occurred at $t = 11$ and 42 µs, with corresponding Hall current local maxima at $t = 20.75$ and 52.75 µs. The average lag between the maxima was therefore 10.25 µs. The breathing mode frequency in this case was 31 kHz for both datasets.

The third breathing mode test case combined data from the magnetic sensor, emissive probe, and high-speed camera. Figure 4.5 shows the projected channel plot for the third breathing mode test case. Note the darkened band from post-processing removal of the emissive probe optical emission. Figure 4.6 compares the Hall current

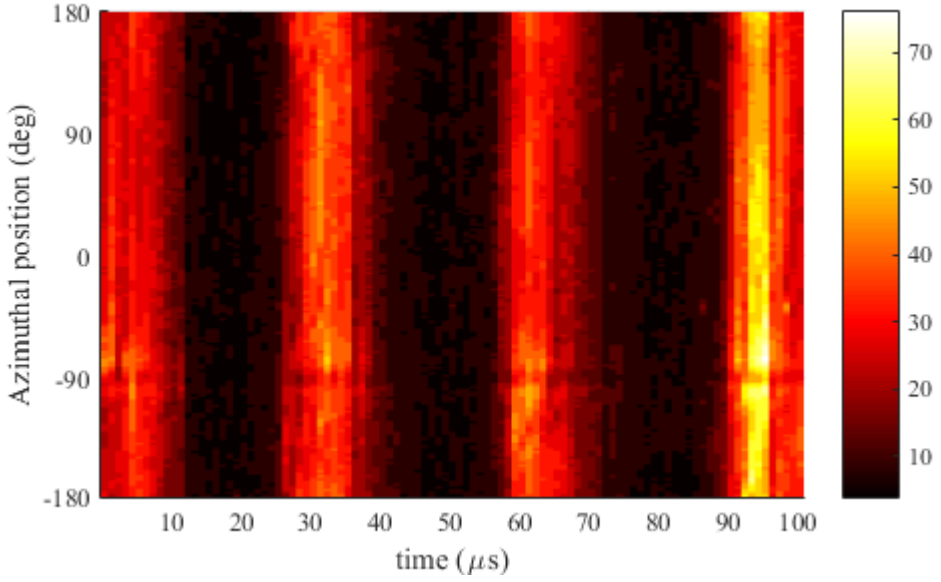

Figure 4.5: Breathing mode test 3 projected channel plot. Arbitrary intensity.

data with the direct emission data. Video maxima occurred at $t = 1, 30, 61$, and 95 µs, while Hall current maxima occurred at $t = 10.75, 40.75$ and 70.75 µs. The average delay between maxima in each dataset was here 10.1 µs. Figure 4.7 compares the video data from $\theta = -80°$ in Fig. 4.5 with the emissive probe floating potential. Local maxima in the emissive probe dataset occurred at $t = 32.27, 62.96$, and 96.34 µs for an average delay between video and emissive peaks of only 1.19 µs. However, note that only one case contains a comparison between video and emissive data. Therefore, the trigger uncertainty in the camera implies the actual delay between emissive and video peaks may rest anywhere in the range from 0.19-1.19 µs. The breathing frequency of

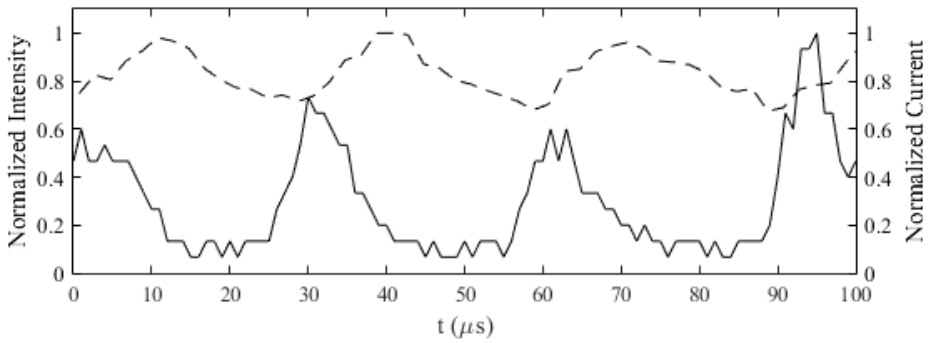

Figure 4.6: Breathing mode test 3 magnetic and video data comparison. Solid line: video data. Dotted line: magnetic data.

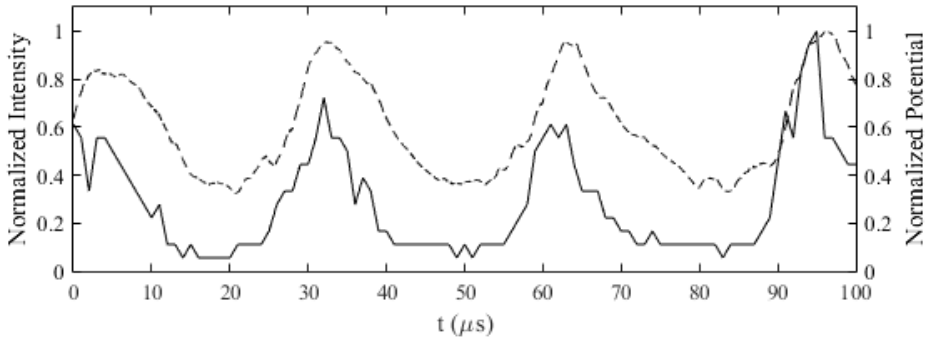

Figure 4.7: Breathing mode test 3 emissive and video data comparison. Solid line: video data. Dotted line: potential data.

the direct emission was 31 kHz, while the frequencies obtained from the Hall current and plasma potential were 31 kHz and 30 kHz, respectively. Finally, Fig. 4.8 compares the normalized video data to the normalized measured discharge current during test 3. There is a close correlation between the breathing in the discharge current and optical emission, as previously established by Liu [40].

The average delay between peaks in direct emission breathing and Hall current breathing across all three cases was 10.9 µs with a standard deviation in the samples of 1.6 µs. The data show a clearly detectable lag between the optical emission of the Hall thruster channel and the magnitude of the Hall current during the breathing mode. This delay apparently does not exist between the optical emission and plasma potential.

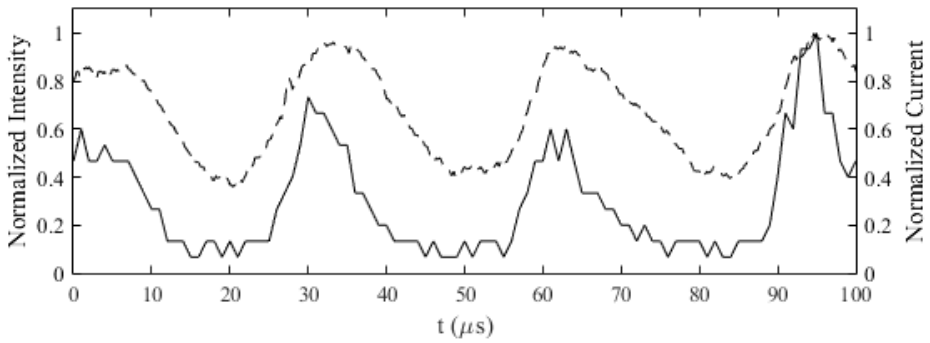

Figure 4.8: Breathing mode test 3 video data and discharge current comparison. Solid line: video data. Dotted line: current data.

4.2 Global Oscillations: Conclusions and Observations

Synchronized measurement of global oscillations led to several conclusions about the breathing mode of the Hall thruster under examination.

4.2.1 Nature of optical emission. The nature of the radiation constituting optical emission in the thruster channel is difficult to determine directly without spectral data, as both excited neutrals and ions emit light due to relaxation after electron bombardment. However, it is possible to infer the cause of optical emission during the breathing mode using synchronized data from multiple sensors. To proceed, assume the discharge current is the sum of the ion beam current, *i.e.* the ion current providing thrust, and the backstreaming electron current from the cathode. Mathematically [1],

$$I_d = I_{ib} + I_{ec}. \tag{4.1}$$

Equation 4.1 is reasonable because current losses other than backstreaming electrons are not measured at the anode. Also note, what was stated as the ion beam current I_{ib} is physically measured as electrons from ionizition events reaching the anode but the two are equivalent due to charge conservation. Additionally, assume the cathode electron current I_{ec} is steady. Therefore, oscillations in the ion beam current map directly to oscillations in the discharge current: $\dot{I}_d = \dot{I}_{ib}$. The ion beam current is due to ions leaving the thruster with velocity v_i. If singly charged ions are assumed for

simplicity, it is possible to write [1]:

$$I_{ib} = -A_c e^- n_i v_i \tag{4.2}$$

where A_c is the channel exit area and for a given power setting, v_i is assumed constant, leaving only the ion density n_i to vary. If multiply charged ions are considered, the total ion beam current is the sum of the currents for each species of ion, each with a different charge and velocity, but the species densities are still the only varying quantities. In Fig. 4.8, a typical case was shown presenting direct emission and discharge current during the same test. Oscillations between the two appear to correlate, as previously shown by Liu [40]. The synchronized oscillation of discharge current with optical emission strongly suggests light emitted during the breathing mode is emitted by ions. It is therefore possible to conclude optical emission of the channel is directly proportional to ion density during the breathing mode.

4.2.2 Relationship between discharge current and Hall current. The consistent phase lag between peaks in the data from Figs. 4.2, 4.4, and 4.6 suggest a relationship between discharge current, direct emission in the channel, and Hall current during the breathing mode. Figures 4.9, 4.10, and 4.11 show the rate of change of Hall current $\dot{I}_H$ compared with the discharge current in each of the three breathing mode cases described in Chapter IV. $\dot{I}_H$ was approximated via backward differencing:

$$\dot{I}_H(t_i) \approx \frac{I_H(t_{i+1}) - I_H(t_i)}{t_{i+1} - t_i} \tag{4.3}$$

and the correlation was emphasized by removing any offset bias in either dataset and normalizing as shown in Eq. 4.4:

$$\mathbf{x_{norm}} = \frac{\mathbf{x} - \bar{\mathbf{x}}}{\max\{|\mathbf{x} - \bar{\mathbf{x}}|\}} \tag{4.4}$$

where $\mathbf{x_{norm}}$ is the conditioned array of data values, $\mathbf{x}$ is the raw array of data values, a bar indicates the mean of the data values, and the absolute value operator in the denominator acts elementwise.

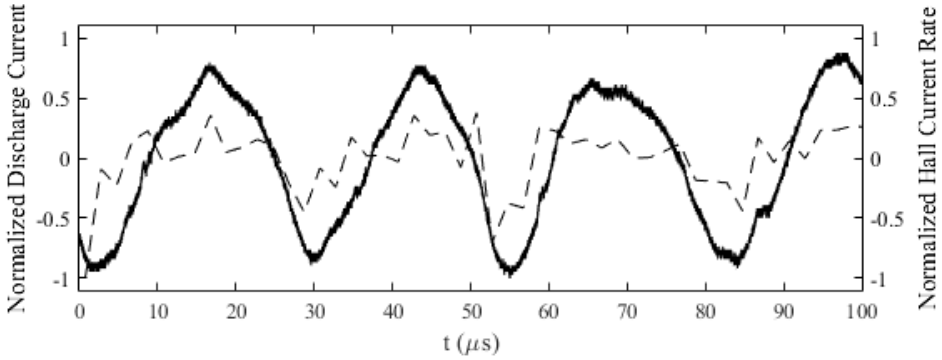

Figure 4.9: Breathing mode test 1 discharge current and Hall current rate comparison. Solid line: discharge current. Dotted line: Hall current rate.

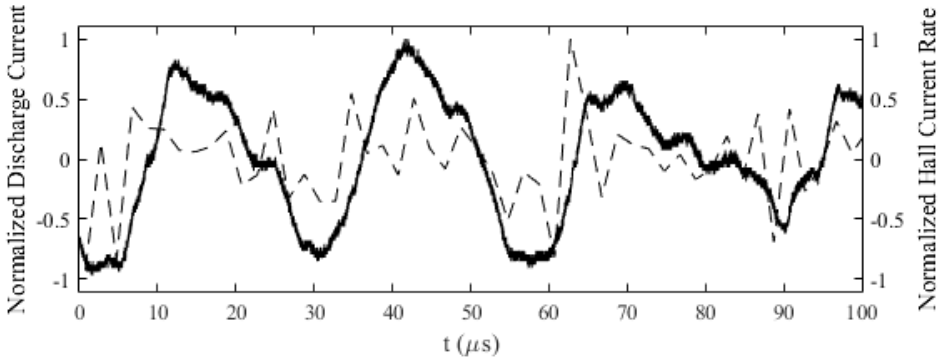

Figure 4.10: Breathing mode test 2 discharge current and Hall current rate comparison. Solid line: discharge current. Dotted line: Hall current rate.

A general correlation is seen between bulk oscillations in I_d and the time derivative of I_H. This relation appears to hold during breathing and some higher order oscillations, up to an additive and a multiplicative constant due to the normalization:

$$I_d \approx \alpha \dot{I}_H + \beta. \tag{4.5}$$

Rather than inferring a purely electrical relationship between these currents, a description based in existing thruster theory of operation serves to explain the observed

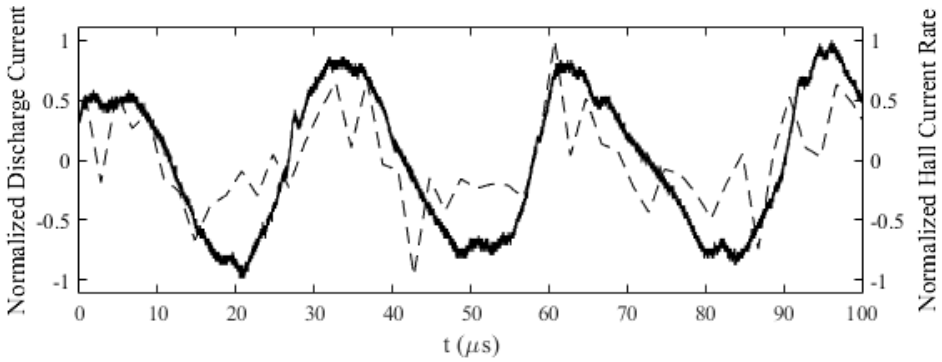

Figure 4.11: Breathing mode test 3 discharge current and Hall current rate comparison. Solid line: discharge current. Dotted line: Hall current rate.

behavior. Recalling the varying portion of I_d was the ion beam current, and recalling Eq. 4.2, we may subsume other constants into α and β to write:

$$n_i \approx \alpha \dot{I}_H + \beta \tag{4.6}$$

This behavior supports the predator-prey cycles such as those of Fife or Yamamoto [25, 41].

In this qualitative description, electrons play the role of predators and neutrals play the role of prey. In the beginning of a breathing cycle, electrons drift in the Hall current with a magnitude approximately 40-50% of maximum, as observed. As neutrals travel downstream, they encounter the Hall current and are ionized once they are of sufficient density to have frequent energetic collisions with drifting electrons. This leads to three phenomena observed in the data: increased optical emission, increased discharge current, and an upward slope, or "inhale," in the Hall current as electrons are freed during the ionization process. As the neutral buildup is depleted, ionization rate and therefore optical emission peaks and then subsides when the neutrals are of insufficient density to sustain ionization. The magnitude of the Hall current continues to climb as long as ionization continues, attaining a maximum when ionization subsides. However, due to the paucity of collisions with neutrals the Hall current gains no new electrons and rapidly depletes, "exhaling" and attaining another minimum.

This allows neutrals to repopulate the ionization zone, restarting the cycle. Figure 4.12 shows a color-coded version of the video/magnetic comparison in Fig. 4.6 with the Hall current inhales and exhales highlighted in red and blue, respectively. During inhales, ionization feeds the Hall current. During exhales, the lack of ionization depletes the Hall current.

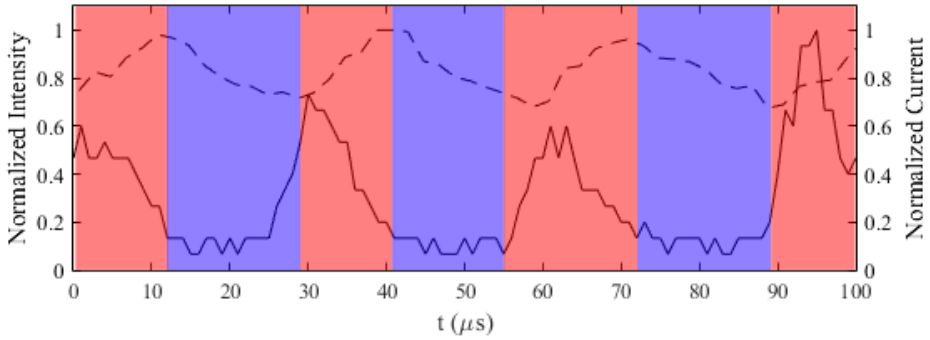

Figure 4.12: Annotated breathing cycle, reproduced from Fig. 4.6. Solid line: video data. Dotted line: magnetic data. Hall current inhale: Red. Hall current exhale: blue.

4.2.3 Plasma potential oscillations during the breathing mode. As a final note on the breathing mode, recall the observed correlation between oscillations in the direct emission and discharge current with oscillations in the plasma potential during breathing. Also recall the result derived in Eq. 4.6, where breathing oscillations in the discharge current and direct emission are associated with ion density oscillations. The measured electric potential is proportional to charge density for fixed geometry in the electrostatic, continuum approximation [5]:

$$V(\mathbf{r}) = \frac{1}{4\pi\epsilon}\int_{Q'}\frac{\rho(\mathbf{r}')}{\|\mathbf{r}-\mathbf{r}'\|}dQ' \tag{4.7}$$

where Q' is the volume under consideration, $\mathbf{r}$ is the location of potential measurement, and $\mathbf{r}'$ is the location of charge distribution in Q'. This approximation holds since the phenomena observed here are well below the plasma frequency so it is reasonable to ignore electrodynamic effects. Thus, regions of higher potential are expected

to correlate with regions of higher ion density, as predicted by Eq. 4.6. This further corroborates the association between ion density and optical emission during breathing, as well as the qualitative description of breathing above. However, the current analysis provides no insight into the existence or proportions of multiple ion species.

4.3 Spoke Oscillations: Data

The majority of test data was collected in attempts to identify trends in plasma behavior during spoke passage. For ease of reading, only selected data is presented below in order to illustrate the analysis process. The complete set of similar plots used to analyze spoke data is collected in Appendix A. First, emissive probe and high-speed imaging data are compared, followed by a similar comparison between magnetic sensor data and high-speed imaging data. Finally, trends in plasma behavior as well as sensor performance are examined.

4.3.1 Selection Criteria for Analysis. Only features clearly identifiable both in projected-channel plots and under examination of individual azimuthal bands of direct emission intensity plots were chosen for analysis. This excluded some spokes visible in the raw video data. Adherence to the following criteria was attempted when selecting spokes for analysis:

1. **Length.** If spokes were not long-lived enough to allow clear identification as azimuthal features, they were not analyzed. This equates to spokes of duration approximately 5 µs or longer.
2. **Prominence.** If spokes were not clearly visible as increases in optical emission followed by a decrease in optical emission, they were not analyzed. This selection criterion is difficult to quantify and may have excluded wide and weak spokes, as well as spokes too strongly associated with rising or falling portions of the breathing mode.

3. **Position.** Spokes analyzed here must have passed either the emissive probe location, the magnetic sensor location, or both. Many spokes only captured via high-speed imaging are not directly analyzed here.

Selection bias associated with these criteria may skew the results. Factors not examined systematically include spoke width and overall duration.

4.3.2 Emissive Probe Data. In total, 36 cases of spoke passage by the emissive probe were selected for analysis. The velocity of each spoke was measured using the pixel translation method outlined in Chapter III. The velocity distribution is shown in Fig. 4.13. The average value 21.9 kHz corresponds to an angular velocity

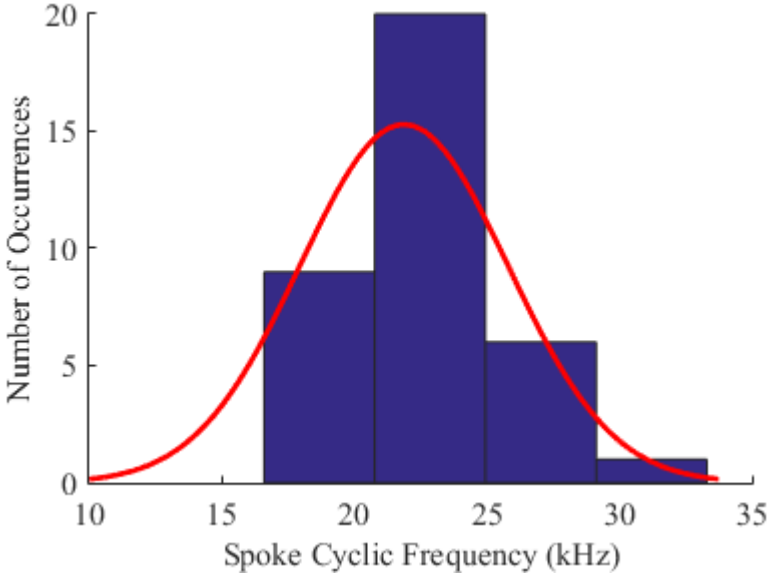

Figure 4.13: Histogram of measured spoke velocities with fitted normal distribution superimposed in red. Sample mean: 21.9 kHz, Sample standard deviation: 3.87 kHz.

of 7.9 deg/µs. Table 4.1 shows a list of all spokes analyzed along with their times of emissive probe passage and their velocity.

Figure 4.14 is a projected channel plot showing clear spoke activity passing by the emissive probe and the magnetic sensor. The prominent spoke beginning at the lower bound of the plot at around $t = 25\,\mu s$ and extending to approximately the 90° position at about $t = 50\,\mu s$ will serve as a test case for analysis. This spoke's angular

Table 4.1: List of spokes analyzed at time of emissive probe passage.

Test Number	t_{peak}	Frequency (kHz)	velocity (deg/μs)
2	2.7	22.2	8.0
2	91.8	22.2	8.0
3	81.9	25.0	9.0
4	49.8	22.2	8.0
4	56.8	22.2	8.0
4	60.8	22.2	8.0
5	41.8	22.2	8.0
5	47.3	22.2	8.0
5	72.8	22.2	8.0
6	0.8	22.2	8.0
6	7.2	33.3	12.0
6	14.8	16.6	6.0
6	79.8	22.2	8.0
6	87.9	25.0	9.0
7	17.8	22.2	8.0
7	32.3	22.2	8.0
7	39.8	22.2	8.0
8	20.8	22.2	8.0
8	31.0	27.7	10.0
8	37.0	27.7	10.0
10	2.3	16.6	6.0
10	14.3	16.6	6.0
10	21.3	16.6	6.0
10	83.8	22.2	8.0
10	93.3	22.2	8.0
11	3.0	27.7	10.0
11	8.0	27.7	10.0
11	14.3	16.6	6.0
11	24.8	22.2	8.0
11	28.8	22.2	8.0
14	30.8	16.6	6.0
14	35.3	16.6	6.0
14	90.8	22.2	8.0
14	96.3	22.2	8.0
15	68.8	16.6	6.0
15	72.3	16.6	6.0

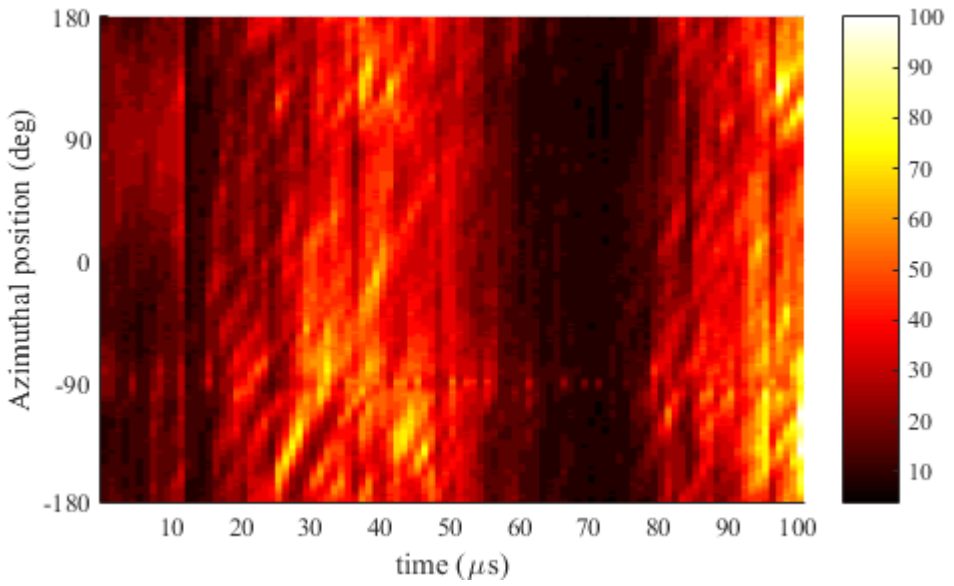

Figure 4.14: Spoke mode test 8 projected channel plot. Arbitrary intensity.

frequency was measured at 27.7 kHz and at any given time it occupies between a 45° and 90° segment of the channel, enabling good characterization of its position. The comparison between the emissive probe reading associated with the spoke's passage and the time compensated video data associated with its passage is highlighted with a red box in Fig. 4.15. From Figs. 4.14 and 4.15 several typical behaviors are observable.

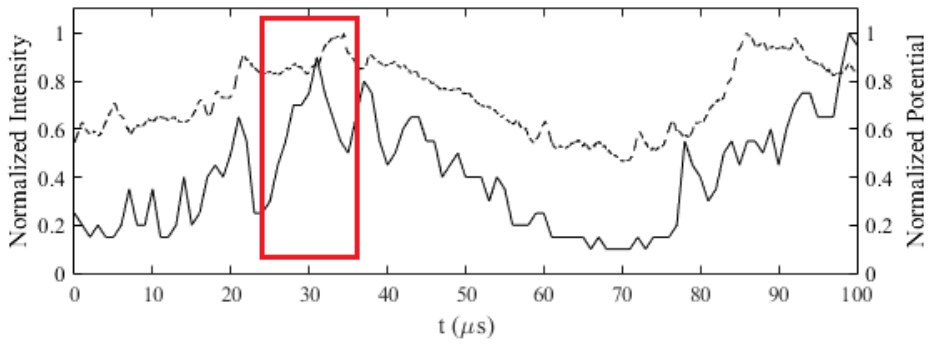

Figure 4.15: Spoke mode test 8 emissive and video data comparison. Solid line: video data. Dotted line: potential data. Spoke under examination highlighted with red box.

First, spokes occur as a superposition on top of the breathing mode. Note the breathing mode has lower frequency due to the reduced discharge potential, as found

previously [40]. Only 12 of the spokes analyzed were strongly associated with the rising edge of the breathing mode, while the other 24 were either associated with the falling edge or not strongly associated. This indicates there is no correlation between the spoke mode and breathing mode. Second, there is not a one-to-one relationship between higher frequency oscillations in the plasma potential and visible spoke passage, and potential oscillations occur even during the darkest periods of optical emission. Strong oscillations in the dark regions are visible in Fig. 4.15, but were especially prevalent in test 15, as shown in Fig. 4.16 below. Third, spokes are

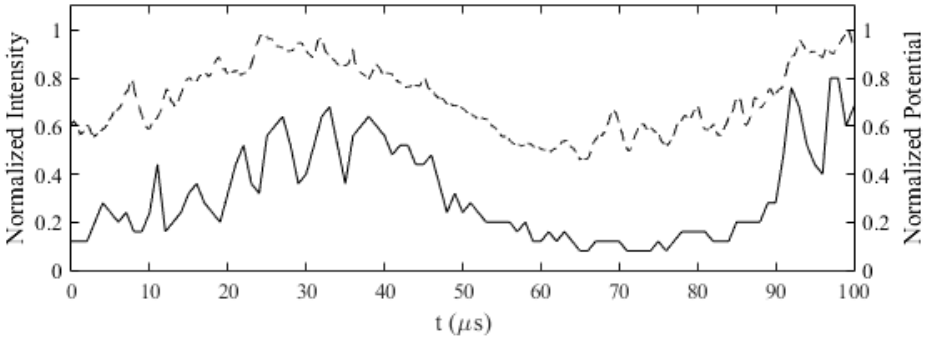

Figure 4.16: Spoke mode test 14 emissive and video data comparison. Solid line: video data. Dotted line: potential data. Note strong oscillations in plasma potential during the period of lowest optical emission from $t = 60$ to 80 µs.

observed to travel in the $\mathbf{E} \times \mathbf{B}$ direction. Fourth, as also seen in the breathing mode cases, plasma potential never decays to less than about 40% of its maximum value.

For each case of spoke passage by the emissive probe, the time of peak direct emission intensity associated with a spoke at the emissive probe was noted and compared against the emissive probe potential measurements. Specifically, the first local minimum and maximum on either side of spoke passage were found. No specific plasma potential pattern was found to correlate with spoke passage. Additionally, the relative delay between local minima and maxima varied substantially from spoke to spoke, obscuring any underlying structure. However, in 22 of 36 cases the spoke's peak was closer to a local plasma potential minimum than a local plasma potential maximum. Additionally, in 31 of 36 cases the spoke's peak or falling edge was as-

Table 4.2: List of spokes analyzed at time of magnetic probe passage.

Test Number	t_{peak}
2	14
3	92
5	51.5
6	89
7	37
7	93
8	39
8	93
10	17
12	25
12	81.5
15	62
M-4	45
M-5	45
M-5	51
M-8	14
M-8	19
M-11	69
M-11	74
M-13	33

sociated with a rising plasma potential. The 5 cases where this association was not observed all occurred on the falling edge of a breathing mode cycle, where any rise in the plasma potential appeared masked by larger thruster oscillations as seen in Figs. 4.15 and 4.16.

4.3.3 Magnetic Sensor Data. Despite sensor limitations, data from 20 spokes passing the magnetic sensor was isolated using the same criteria applied for the emissive probe. The spokes analyzed are listed in Table 4.2. Test runs preceded by an M were performed on a day when the emissive probe was not used. Again, an illustrative case is included here while the rest of the relevant plots are located in Appendix A. Figure 4.17 shows the Hall current solution compared with the video data from $\theta = 0^\circ$ of test 8, as shown in Fig. 4.14.

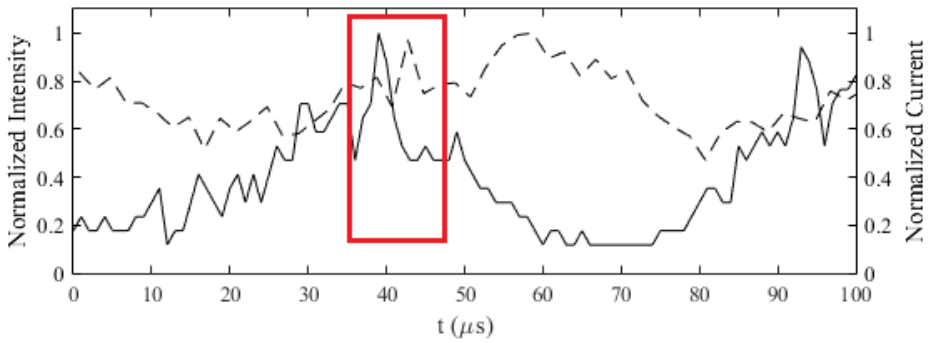

Figure 4.17: Spoke mode test 8 magnetic and video data comparison. Solid line: video data. Dotted line: current data. Spoke under examination highlighted with red box.

In Fig. 4.14 the spoke's maximum and a local maximum in the Hall current appear to occur simultaneously, followed by decay and a larger spike in the Hall current associated with the passage of the spoke. Spoke decay was associated with rising Hall current in 13 of 20 cases. As with the emissive probe data, it was difficult to identify any more specific pattern due to the uncertainty in the data. Nevertheless, the Hall current tentatively shows similar behavior to the plasma potential during azimuthal oscillations.

4.4 Spoke Oscillations: Conclusions and Observations

The results obtained regarding the breathing mode do not necessarily apply during azimuthal plasma oscillations and interesting trends were observed during the present experiments. General spoke properties from video analysis are discussed below, followed by inferences about behavior from the synchronized data. The structure of a spoke is argued to consist of several discrete parts. Since the only sensor with azimuthal resolution was the high-speed camera, discussions of spoke origin and duration are related to the observable optical emission of the spokes. Additionally, as set up above the visible part of a spoke is used as a reference for the relative location of other parts of the spoke.

4.4.1 Direction. All spokes observed in tests conducted for this research moved in the $\mathbf{E} \times \mathbf{B}$ direction. This is in agreement with Janes and Lowder, Liu, Sekerak, and others [12, 28, 42]. Time resolved experiments by Smith and Cappelli have observed spokes rotating in the opposite direction [26]. However, their results are difficult to compare to the present research due to a dissimilar test method. Oscillations propagating in the $\mathbf{E} \times \mathbf{B}$ direction are consistent with current density fluctuations in the larger overall Hall current structure.

4.4.2 Velocity. The spokes observed in the current experiments traveled with an average velocity corresponding to azimuthal spokes observed in other experiments, as illustrated in Fig. 4.13. The present average value of 22 kHz compares well with Sekerak *et. al*'s average value of 20 kHz and Liu's distribution between 14-75 kHz [40, 42]. Note the dependence of azimuthal spoke velocity on thruster operating parameters is well characterized elsewhere, e.g. by Janes and Lowder, Liu, and Sekerak *et. al*, and was not under investigation during the present research [12, 40, 42].

4.4.3 Origin and Duration. Spokes were observed to originate around the entire thruster face. However, the lower half of the thruster face from $-180°$ to $0°$ appeared to contain the origin of many more spokes than the upper half. This bias in origin location occurred during tests both with and without the emissive probe. This is possibly due to the cathode position at $-180°$, as the cathode position is the only obvious asymmetry in the thruster geometry. As electrons from the cathode become trapped in the Hall current, they travel preferentially in the $\mathbf{E} \times \mathbf{B}$ direction, counterclockwise in the present research. The bias in spoke origin location may indicate that nonuniform cathode electron generation behavior contributes to spoke generation. Less obvious asymmetries in the thruster may also provide an explanation for this behavior, including nonuniformities in the magnetic field, neutral flow, or a region of increased electron emission near the walls. Further testing is necessary to determine the spoke start location bias.

4.4.4 Clustering. Spokes were sometimes observed to occur in clusters spanning up to approximately 90° of the thruster face. Notably, the spokes did not appear to take up the entire channel at once. Azimuthal features in the thruster appeared to move with the same velocity during the same instance, suggesting a cohesive structure. However, there were cases when very high frequency azimuthal features not analyzed here appeared to exist at the same time as, and overtake, azimuthal spokes. The breathing mode and spoke mode are seen to exist simultaneously, and there is no reason to exclude the possibility of even higher order oscillations occurring at the same time as well. Indeed, this is consistent with other observations of multiple plasma instabilities existing simultaneously [23]. These faster features may have occurred at a different axial location in the thruster than the spokes under examination.

4.4.5 Structure. A strong correlation between the visible emission of a spoke and an increase in plasma potential was observed. Namely, after the peak brightness in the visible part of a spoke passed by the emissive probe, an increase in plasma potential was almost always detected. To interpret this result, assume a spoke is an azimuthally varying feature rotating with constant velocity but otherwise fixed on the timescales considered. In this case, it is possible to find a reference frame with azimuthal coordinate θ' where the potential $V'(\theta')$ is at rest but the azimuthal variation of the potential is nonzero. Such a frame is moving with a constant velocity relative to the thruster reference frame, namely the spoke velocity $\dot{\theta}$. In this case, at a constant sensor location in a frame at rest with respect to the thruster a time-varying potential $V(t)$ is measured. As shown in Appendix B the transformation between these two frames is:

$$V(t) = V'(-\dot{\theta}t). \tag{4.8}$$

As also shown in Appendix B, given Eq. 4.8,

$$\frac{dV'}{d\theta'} = -\frac{\dot{V}}{\dot{\theta}}. \tag{4.9}$$

From now on, the primes are dropped because azimuthal features in the primed frame are also azimuthal features in the unprimed thruster frame. Recalling the definition of electric potential in cylindrical coordinates:

$$E_\theta = -\frac{1}{r}\frac{\partial V}{\partial \theta} \tag{4.10}$$

the following relation should hold for spokes as long as $\dot{\theta}$ is constant and positive, for constant r:

$$E_\theta \propto \dot{V}. \tag{4.11}$$

Hence, the visible emission of the spoke is associated with a region of azimuthal electric field as first observed by Janes and Lowder, allowing anomalous electron transport to the anode through axial drift currents [12]. Figure 4.18 shows the implied spoke structure based on observational trends and the electrostatic approximation.

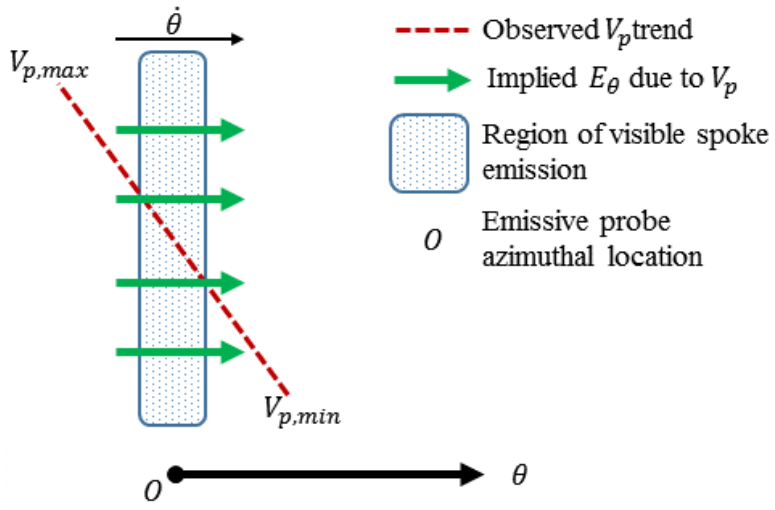

Figure 4.18: Notional spoke structure derived from experimentally observed trends.

Additionally, the region of low potential azimuthally preceding the spoke emission indicates more negative charge distribution, with more positive charge distribution following the visible spoke emission. This could indicate visible spoke emission is at least partially due to ions, not high energy neutrals. It could also indicate the azimuthal electric field observed is due to a local charge structure with electrons pre-

ceding ions traveling in the azimuthal direction. However, there are potential issues with inferring such a structure as detailed below.

4.4.6 Additional Notes on Spoke Behavior. The types of plasma potential oscillations associated with spoke passage during optical emission were also observed during gaps in thruster emission. Although it is impossible to positively associate these oscillations with spokes due to the use of only a single means of detecting plasma potential, their presence is suggestive of similar interesting plasma structures occurring independent of the thruster breathing. Indeed, spokes appear to begin throughout the breathing cycle when there is optical emission, although the brightest regions are often most easily observed. A second synchronized means of plasma potential measurement could confirm or exclude the possibility of spokes when the thruster is not emitting optically.

It is also important to note another ambiguity. Although optical emission appears to imply ionization in the phenomena studied, ionization may also occur without causing optical emission detectable by the high-speed camera. The combination of the emissive probe oscillations in the dark periods of videos with the inability to resolve ionization processes during the same periods makes any inference of ion position within a spoke structure tentative.

Magnetic sensor data from spoke passage was noisy and its significance is difficult to interpret. Using a steady current assumption to solve for features with known azimuthal variation complicates the association of sensor output with physical phenomena. However, there was a weak trend supporting an increase in Hall current after the visible passage of spokes by the sensor. It is unclear what the trend implies, or indeed if the trend is due to the solution method or thruster behavior.

4.5 Comments on Experimental Method

The synchronized measurement of direct channel emission, plasma potential, and Hall current was a novel method developed for the present research. Although

the method was successful for measuring features in the 600 W thruster used, further improvements are possible. The magnetic sensor and emissive probe both impinged on the thruster plume, causing an approximately 5% increase in the discharge current over thruster baseline operating conditions. However, no obvious effect was observed on time-dependent plasma structures in the channel at large due to the emissive probe.

4.5.1 Efficacy of emissive probe. The emissive probe proved an outstanding tool for measuring oscillations in plasma potential, as the noise in emissive probe measurements was much smaller than the effects under investigation. However, the reliability of the emissive probes was low due to burnout and only one in six probes used operated in the thruster plume long enough to collect any data. The others either became excessively heated by their own resistance or were compromised by exposure to the thruster plume. In order to obtain data on spokes as they occurred, the emissive probe was placed very close to the thruster exit plane. Moving the sensor farther away from the thruster may increase probe lifetimes in the future.

4.5.2 Efficacy of magnetic sensor. The magnetic sensor was designed for use with a larger thruster [34]. As such, the signal to noise ratio of the sensor with the 600 W thruster used in the present research was lower than designed. Additionally, the magnetic sensor's solution method for obtaining the Hall current was designed to provide information about thruster behavior on much longer timescales than those examined here, *i.e.* minutes [38]. The longer timescale increased the validity of assuming steady, axisymmetric Hall currents in the thruster.

However, the use of the magnetic sensor for detecting azimuthal features explicitly violates these two contingent assumptions, throwing doubt on the validity of using the magnetic sensor to study spokes. Nevertheless, as outlined in Chapter IV, trends visible in the data appear to show some azimuthal features in the Hall current were captured by the magnetic sensor's solution. The weak trends observed make the interpretation of data from any individual spoke event difficult.

In the case of the uniformly oscillating breathing mode, the magnetic sensor appeared to perform in a repeatable way as seen in Chapter IV. The breathing mode was also observed by Mullins using the magnetic sensor in a separate thruster [34]. The magnetic sensor displays good utility for measuring uniform current phenomena in thrusters of sufficient size.

4.5.3 Extension to other thrusters. Limited testing conducted with a smaller 200 W thruster as stated in Chapter III showed the present test method is not extendable to smaller thrusters without modification. Although video data was adequate, no synchronized sensor data was useful in analysis. First, due to burnout problems as noted above, no emissive probe data was collected on the smaller thruster. The increased plasma density in the near-thruster plume due to the smaller geometry may have contributed to this problem. Second, the field induced by the smaller Hall current of the 200 W thruster proved too weak for the magnetic sensor to detect with any time resolution. In summary, geometric problems prevent both emissive and magnetic sensor measurement without significant modification of the experimental apparatus.

4.5.4 Cold probes. All attempts to collect plasma potential data with the cold probe setup shown in Fig. 3.12 were beleaguered by a large amount of high frequency noise. Digital filtering or analysis in the frequency domain was considered, but the loss of time-resolution implied made the process infeasible. A more sophisticated cold probe is necessary to obtain comparable results to the emissive probe performance.

V. Conclusion

5.1 Summary of Results

Both the global breathing mode and local azimuthal mode of Hall thruster discharge oscillation were discovered in the initial studies of thruster behavior in the mid-20$^{\text{th}}$ century. However, recent advances in high-speed imaging and thruster diagnostics have opened a new avenue for examining the time-resolved behavior of Hall thrusters during these oscillations. In the present research, high-speed imaging was combined with emissive probe measurements of plasma potential and magnetic sensing of the Hall current at effective resolutions up to 1 µs to observe a commercially available 600 W Hall thruster. This new method allows construction of a more complete picture of plasma behavior during global and local oscillations of the thruster discharge.

During the breathing mode, oscillations in the Hall current were observed to lag oscillations in the direct emission, plasma potential, and discharge current. This relationship was shown to support the existing predator-prey model of breathing mode behavior, while providing additional insight into the dynamics of the Hall current during breathing. Additionally, the direct emission was seen to exhibit behavior consistent with emission of ions rather than energetic neutrals when compared with measurement of plasma potential and discharge current. Obtaining information about the existence of multiple species during specific phases of the breathing mode was complicated by the low density of the plasma and neutral gas throughout thruster operation.

Spokes were observed in high-speed imaging to occur in clusters and to preferentially begin on the lower half of the thruster face. Additionally, plasma potential behavior during observation of the spoke mode was suggestive of spokes even when the thruster was not emitting optically in the range detectable by the camera used. Spokes were further observed to travel exclusively in the $\mathbf{E} \times \mathbf{B}$ direction. While only spokes traveling with frequencies up to 33.3 kHz were examined here, azimuthal features traveling with much higher frequency were also observed to exist at the same

time as the oscillations under analysis. It is not possible to determine from the data whether these fast features existed in the same location axially as analyzed spokes.

During the azimuthal mode, a strong correlation was observed between optical emission of the plasma and a rising slope of plasma potential. Under appropriate assumptions, this was shown to support an azimuthal electric field as observed by Janes and Lowder. This correlation was also indicative of a charge distribution structure within the spoke. The potential behavior combined with the optical emission suggests spoke emission is associated with ions rather than high energy neutrals, possibly pointing to a separation of charge during spokes.

5.2 Next Steps

Multiple avenues are apparent for the researcher wishing to build on the current effort, both experimentally and theoretically. First, the experimental setup used appears readily adaptable to a larger thruster. This would likely provide higher-fidelity magnetic data due to the larger induced magnetic field of a stronger Hall current. Replicating or refuting the current results with a different thruster can provide additional clarity about the phenomena observed here. Next, the experimental method is potentially extendable to smaller thrusters but a new magnetic sensor specifically adapted to the weaker fields is necessary. Additionally, evidence of radial spoke structure was previously observed [40]. Further investigation of radial spoke behavior with synchronized measurement setups, including an improved Hall current sensor, could provide fruitful physical information about spoke structure. Such experiments are theoretically achievable with current technology.

The accuracy of solving for Hall current with the magnetic sensor in various thruster operating regimes needs further definition. As noted above, examining azimuthal modes with the sensor violates several assumptions enabling current solution. Even during steady thruster operation, the boundary conditions used to relate sensor output to current neglect significant physical processes of thruster operation, includ-

ing electron emission and absorption from thruster walls. It is not clear whether such improvements are readily achievable.

A more sensitive and faster high-speed camera could continue to reveal new features of thruster emission. Evidence for higher frequency azimuthal features near the sample rate of the camera was observed in the current research, and investigation into these features may provide better understanding of thruster operation. Higher framerate and shorter exposure times may even yield new insight into the spokes analyzed in the current research. Additionally, the ability to examine ionization behavior through optical emission during the darker portions of thruster breathing is potentially achievable with a more sensitive imager. These experiments are within the current state of the art.

Finally, theoretical understanding of spoke formation, propagation, and dissipation is poorly understood. Fully three-dimensional modeling of thruster behavior is needed to accurately model spoke formation, propagation, and decay in a physically rigorous way, as analytic solution of the behavior is probably not possible. A high-fidelity model of Hall thruster operation incorporating the electron transport and other plasma behavior due to spokes could streamline the thruster design process, allowing performance improvements through better design.

Appendix A. Plots Used to Analyze Spoke Behavior

A.1 Projected Channel Plots

The following projected channel plots are of tests that include spokes analyzed when attempting to deduce general spoke behavior. Test numbers are associated with the run on test day. All plots have arbitrary intensity.

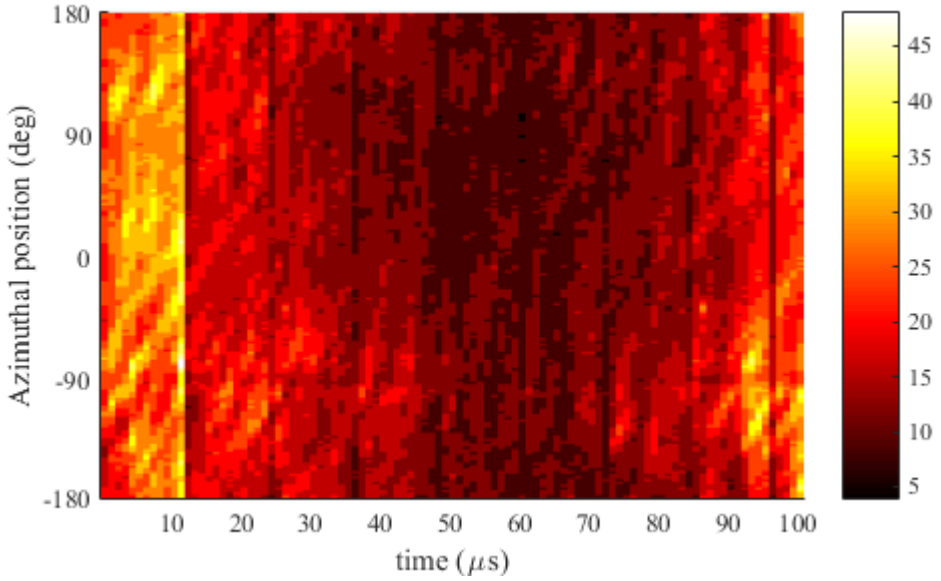

Figure A.1: Spoke mode test 2 projected channel plot.

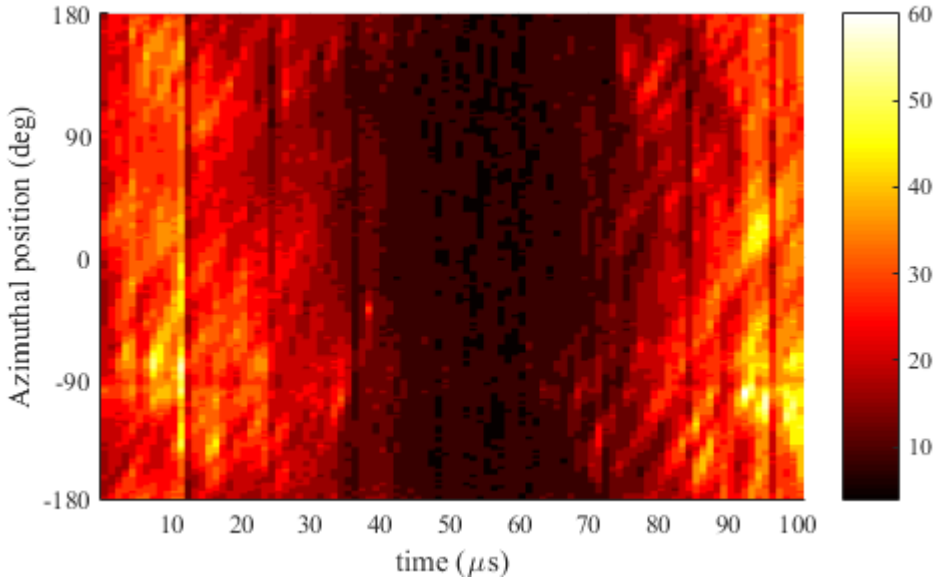

Figure A.2: Spoke mode test 3 projected channel plot.

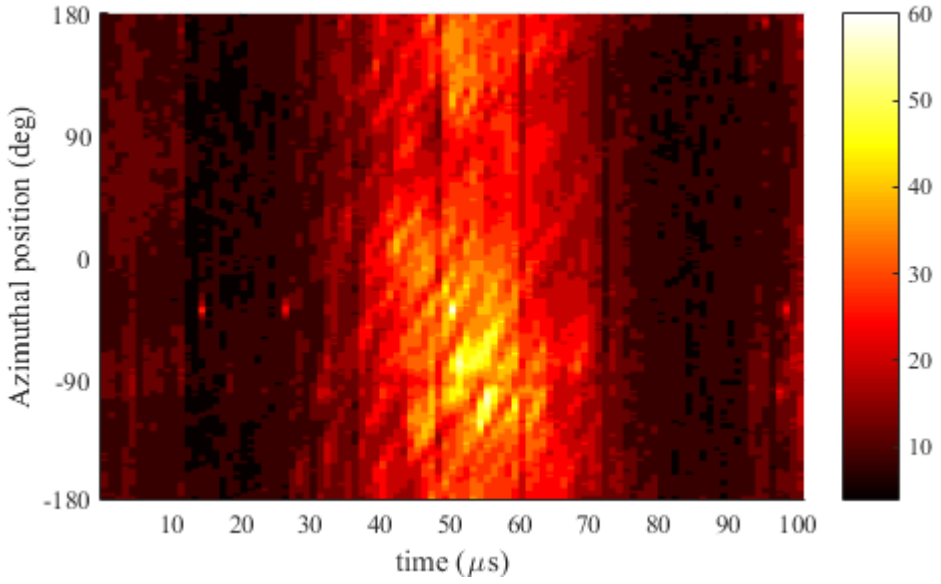

Figure A.3: Spoke mode test 4 projected channel plot.

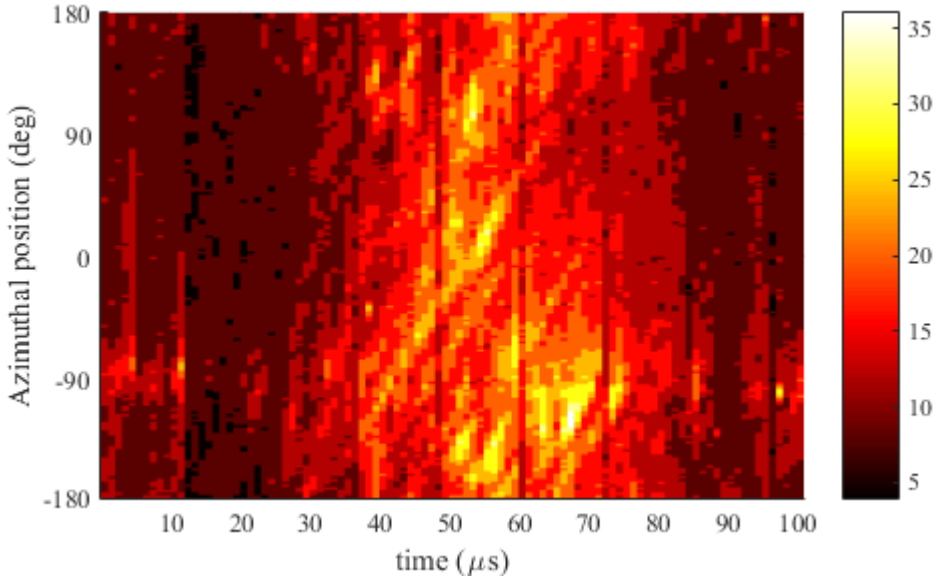

Figure A.4: Spoke mode test 5 projected channel plot.

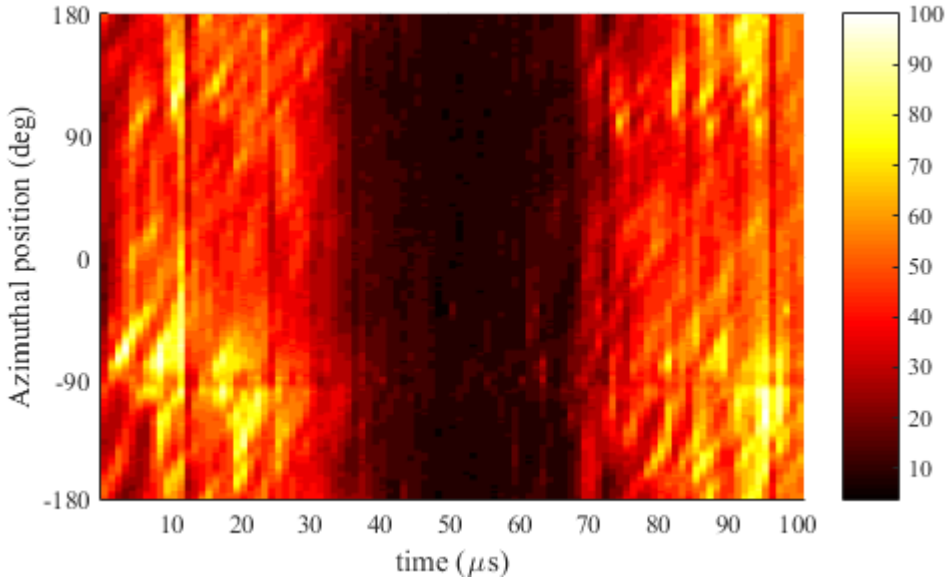

Figure A.5: Spoke mode test 6 projected channel plot.

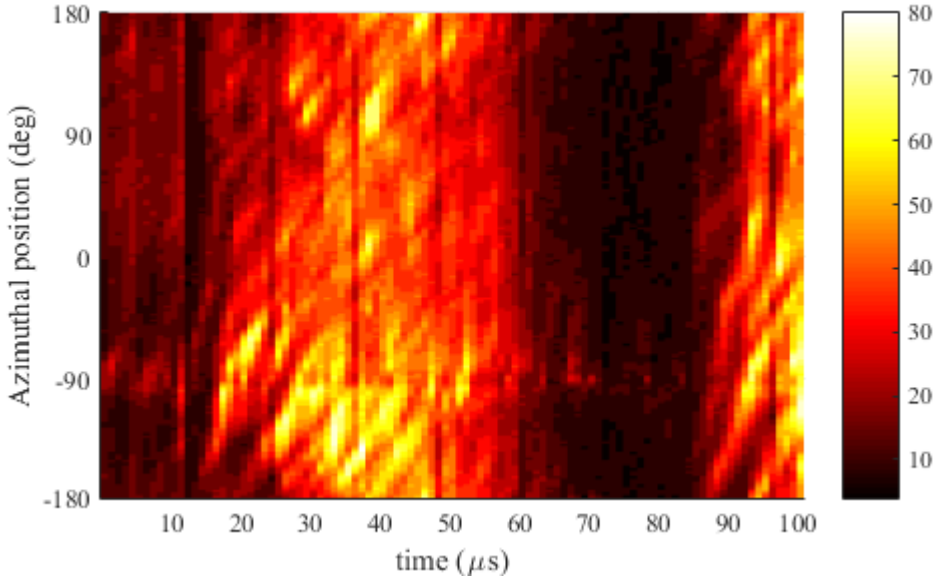

Figure A.6: Spoke mode test 7 projected channel plot.

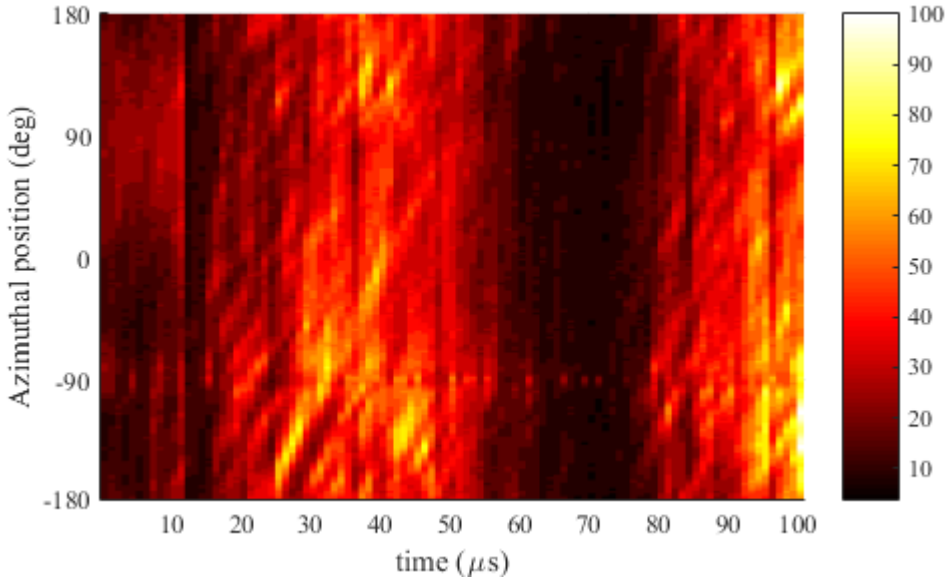

Figure A.7: Spoke mode test 8 projected channel plot.

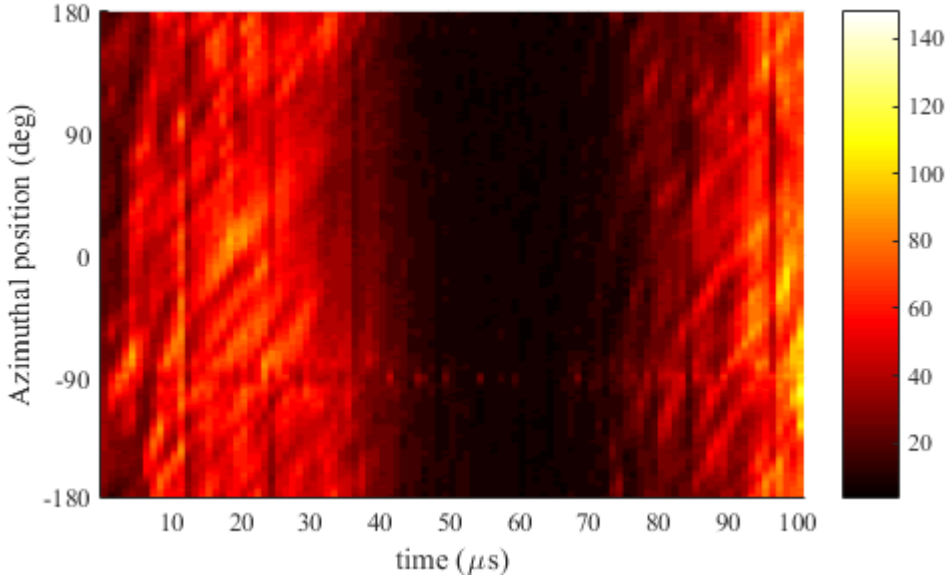

Figure A.8: Spoke mode test 10 projected channel plot.

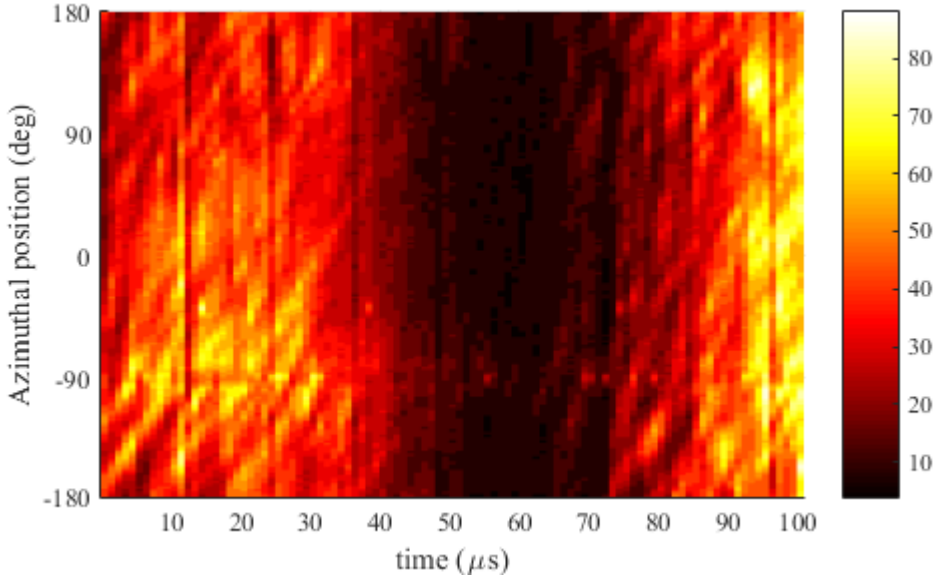

Figure A.9: Spoke mode test 11 projected channel plot.

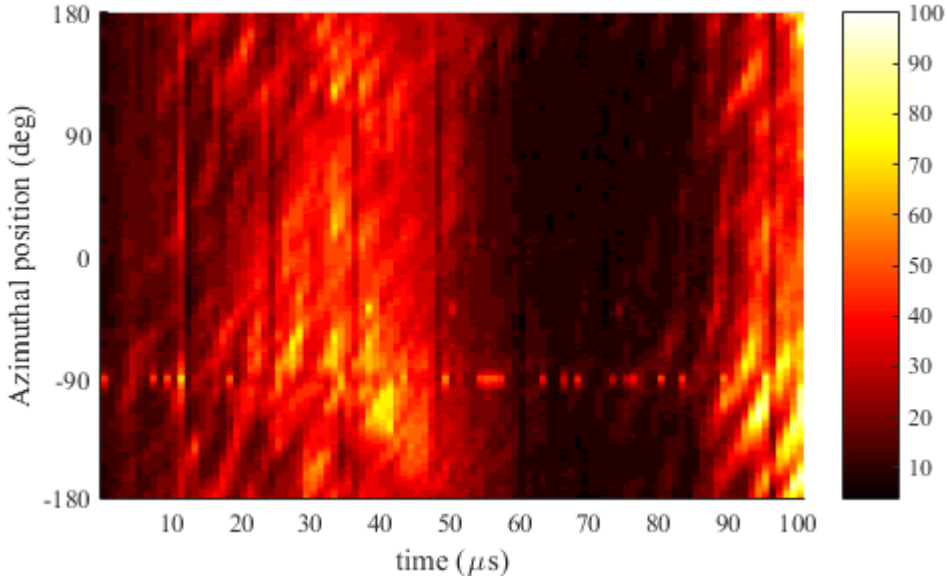

Figure A.10: Spoke mode test 14 projected channel plot.

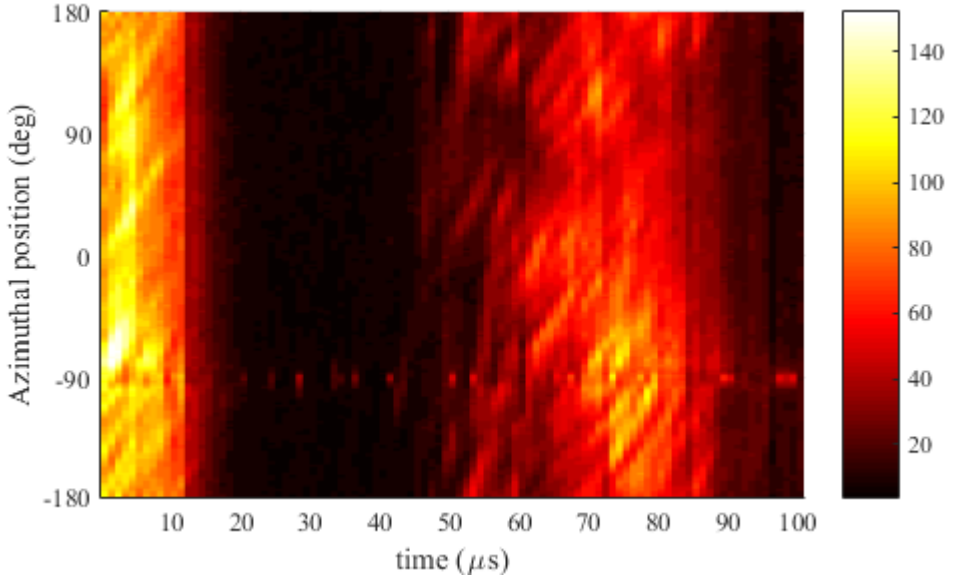

Figure A.11: Spoke mode test 15 projected channel plot.

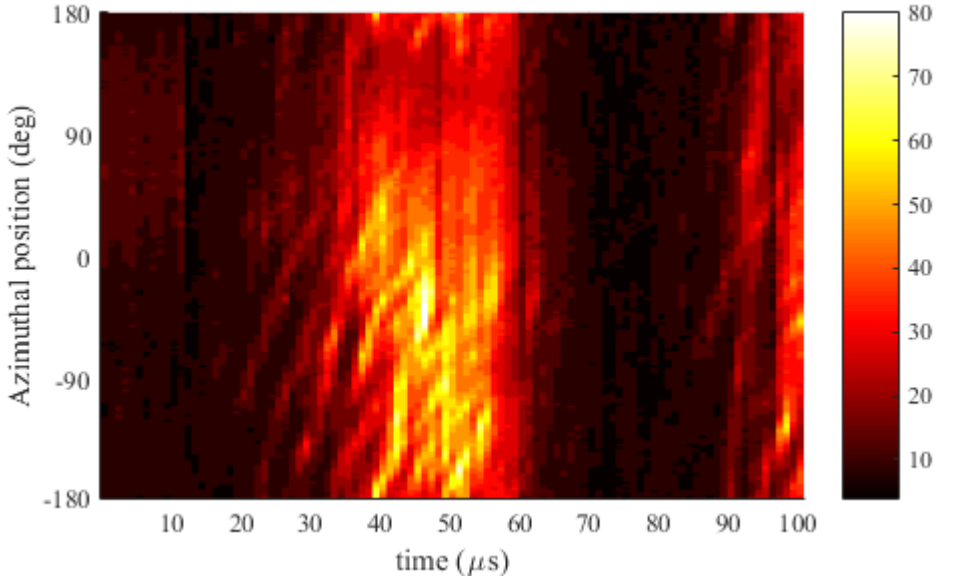

Figure A.12: Spoke mode test M-4 projected channel plot.

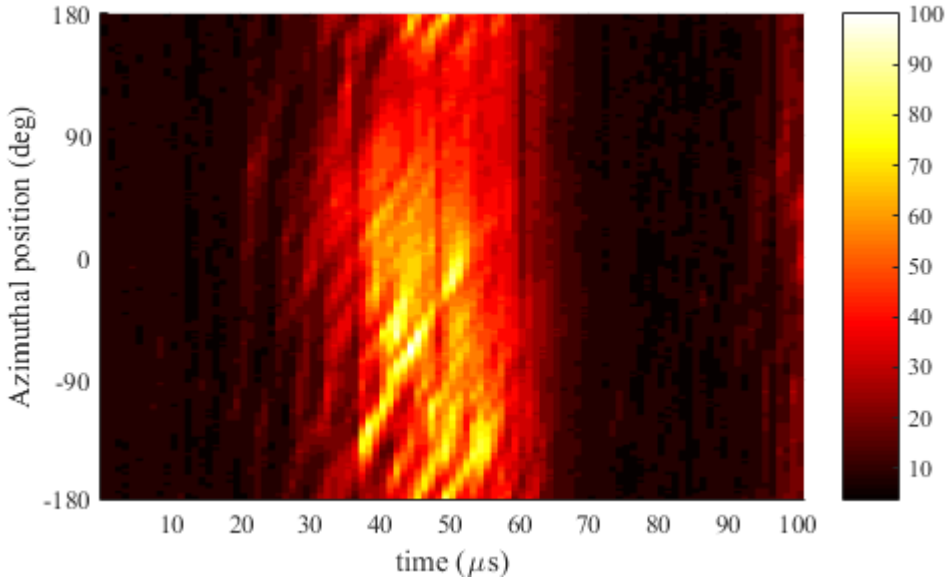

Figure A.13: Spoke mode test M-5 projected channel plot.

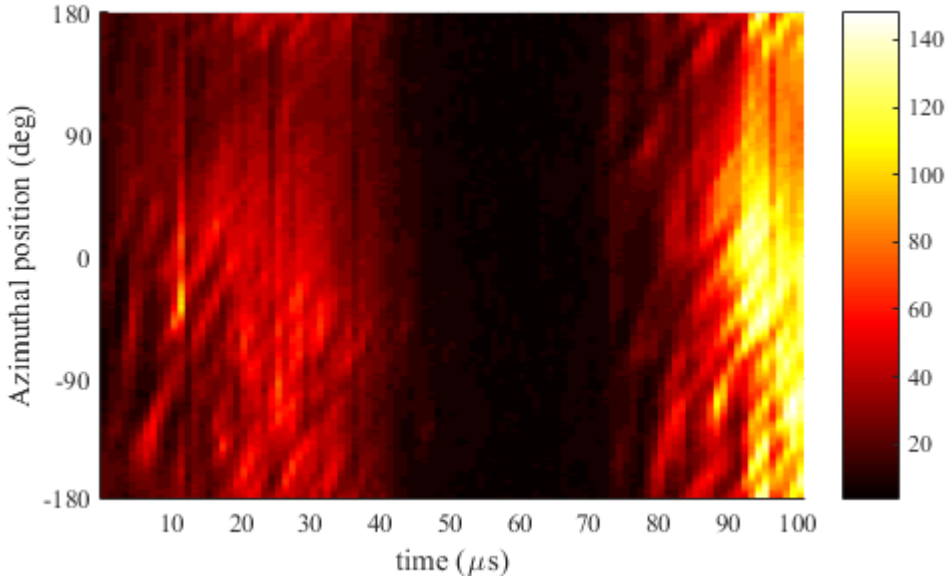

Figure A.14: Spoke mode test M-8 projected channel plot.

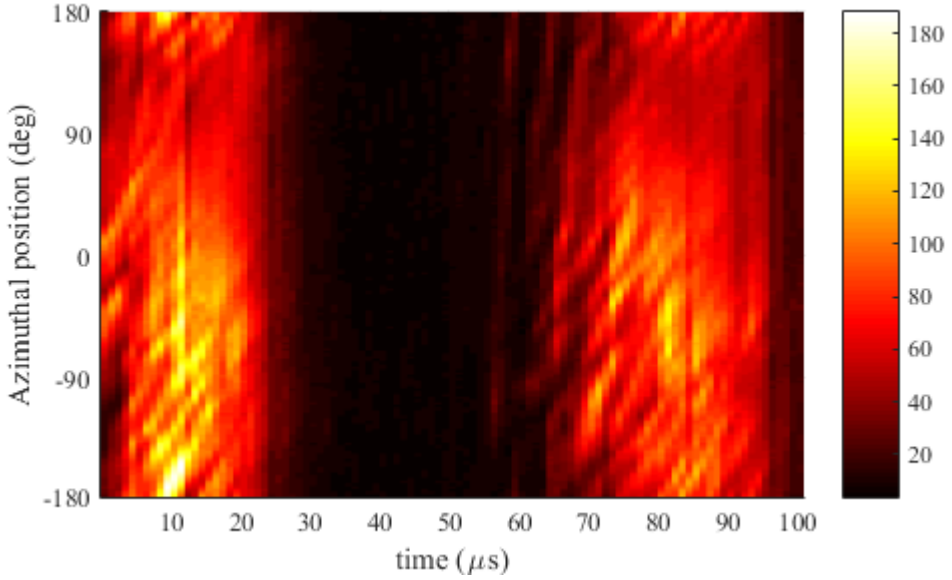

Figure A.15: Spoke mode test M-11 projected channel plot.

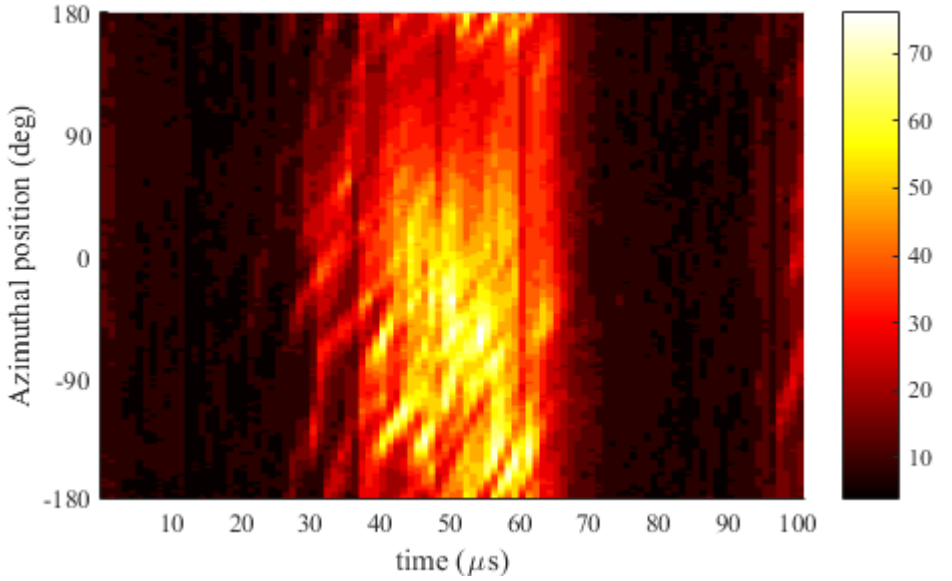

Figure A.16: Spoke mode test M-13 projected channel plot.

A.2 Comparison of Emissive and Video Data

The following plots represent the emissive data from the tests above as labeled, compared with video data from the $-80°$ position on the projected channel plots. No timeshift has been applied to compensate for spoke travel in these plots, to allow similar analysis of all spokes on the same plot. The individual spokes analyzed are listed by video intensity time index in Table 4.1.

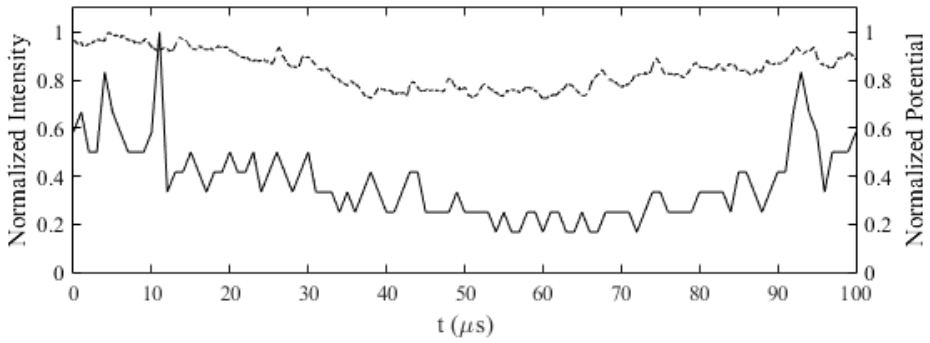

Figure A.17: Spoke mode test 2 emissive and video data comparison. Solid line: video data. Dotted line: potential data.

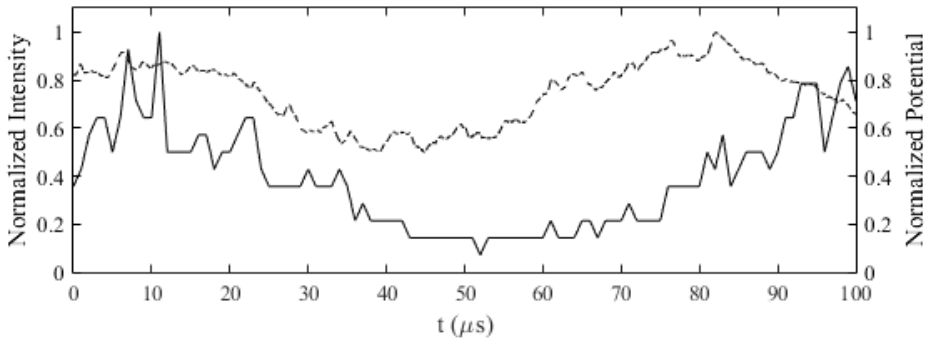

Figure A.18: Spoke mode test 3 emissive and video data comparison. Solid line: video data. Dotted line: potential data.

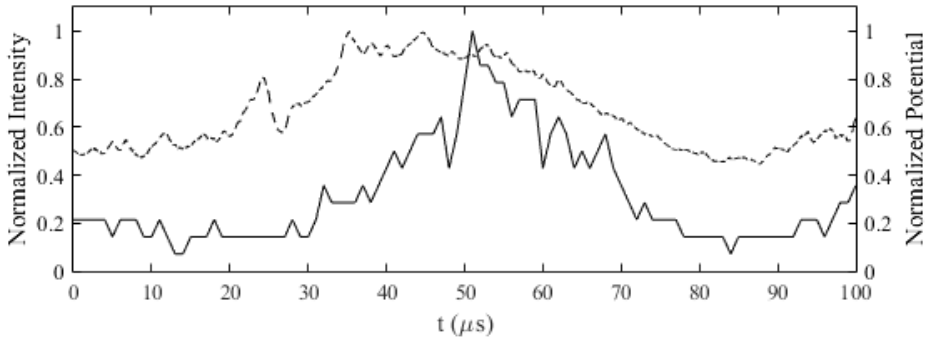

Figure A.19: Spoke mode test 4 emissive and video data comparison. Solid line: video data. Dotted line: potential data.

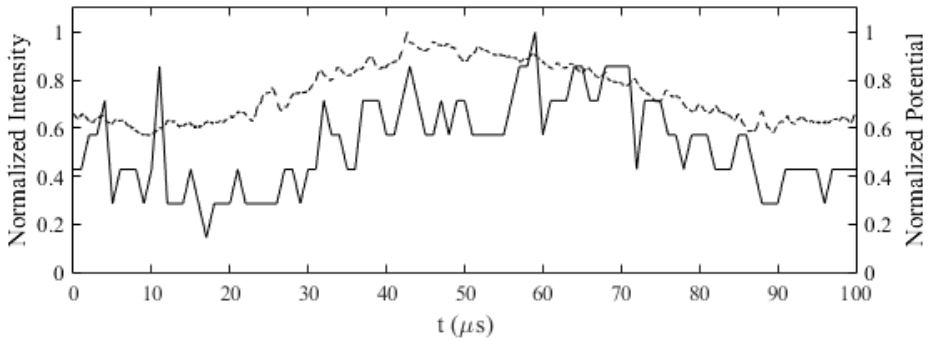

Figure A.20: Spoke mode test 5 emissive and video data comparison. Solid line: video data. Dotted line: potential data.

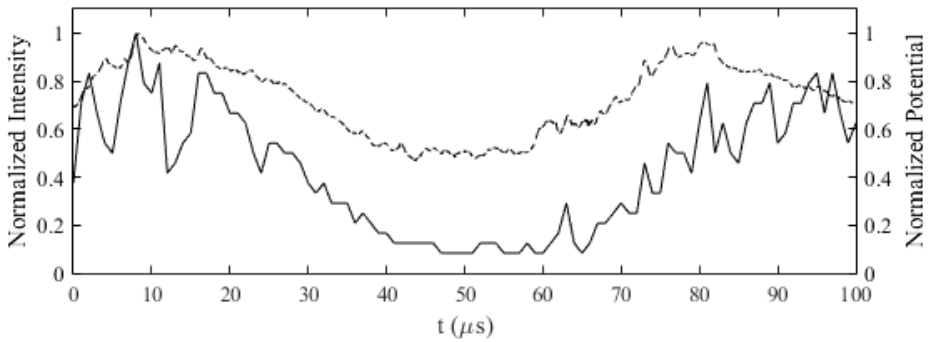

Figure A.21: Spoke mode test 6 emissive and video data comparison. Solid line: video data. Dotted line: potential data.

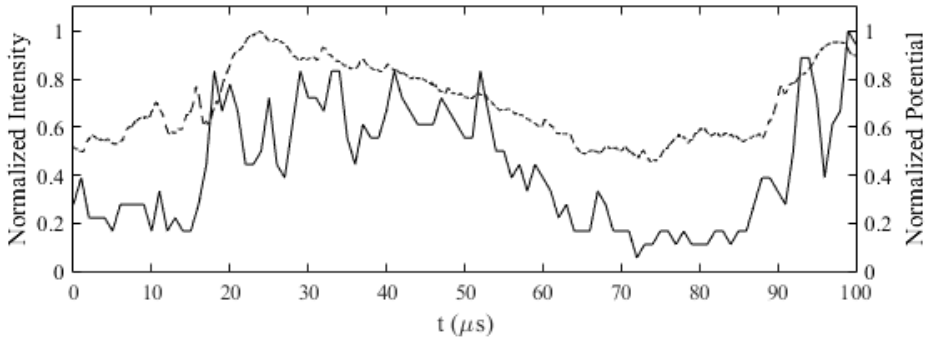

Figure A.22: Spoke mode test 7 emissive and video data comparison. Solid line: video data. Dotted line: potential data.

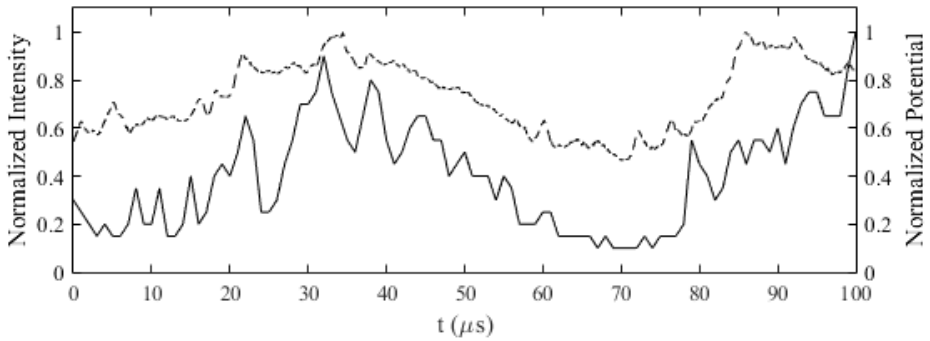

Figure A.23: Spoke mode test 8 emissive and video data comparison. Solid line: video data. Dotted line: potential data.

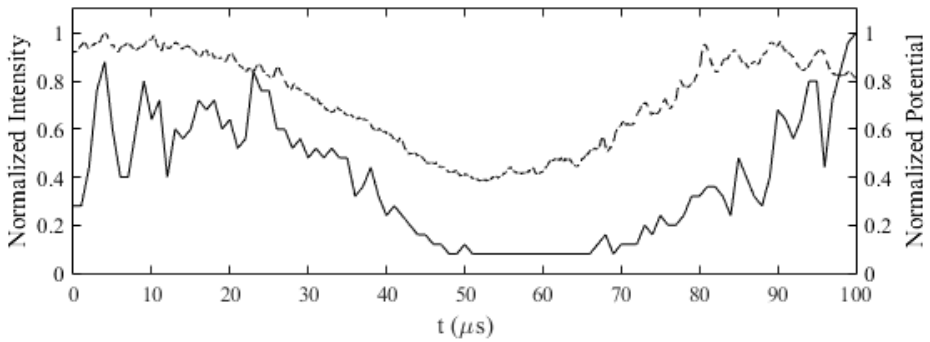

Figure A.24: Spoke mode test 10 emissive and video data comparison. Solid line: video data. Dotted line: potential data.

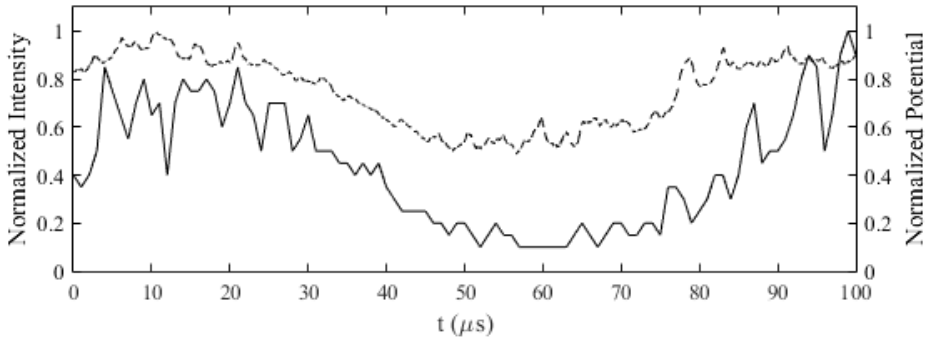

Figure A.25: Spoke mode test 11 emissive and video data comparison. Solid line: video data. Dotted line: potential data.

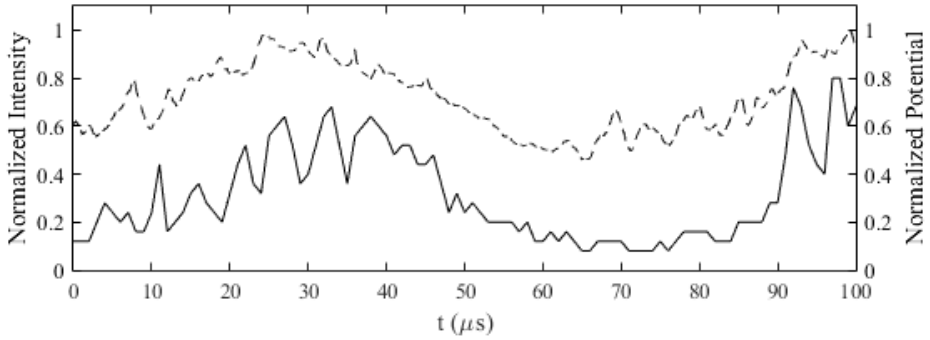

Figure A.26: Spoke mode test 14 emissive and video data comparison. Solid line: video data. Dotted line: potential data.

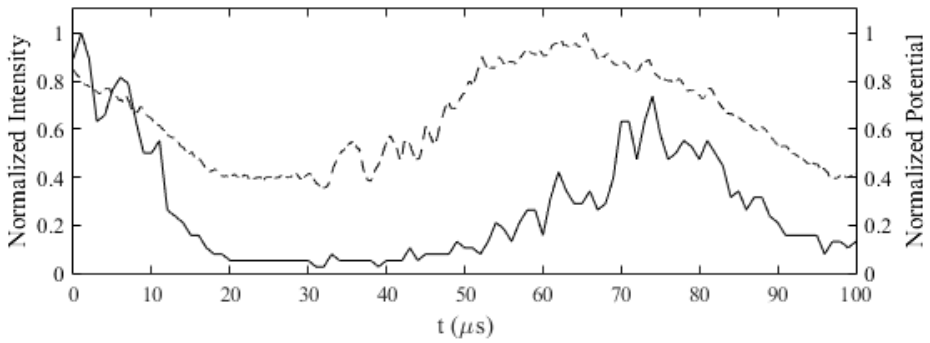

Figure A.27: Spoke mode test 15 emissive and video data comparison. Solid line: video data. Dotted line: potential data.

A.3 Comparison of Magnetic and Video Data

The following plots represent the magnetic data from the tests above as labeled, compared with video data from the 0° position on the projected channel plots. The individual spokes analyzed are listed by their video intensity time index in Table 4.2.

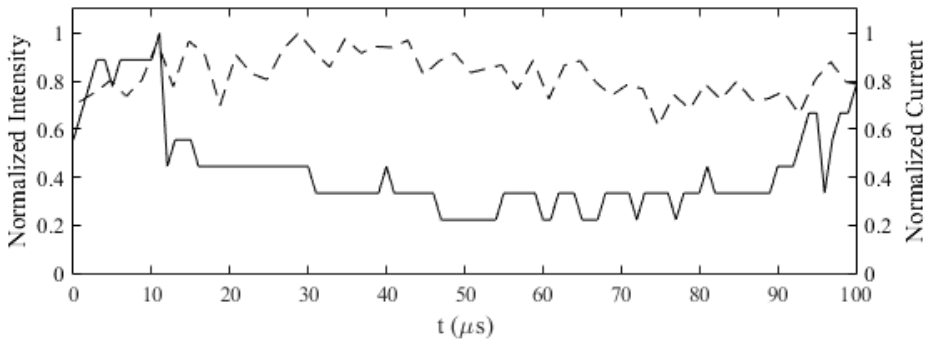

Figure A.28: Spoke mode test 2 magnetic and video data comparison. Solid line: video data. Dotted line: current data.

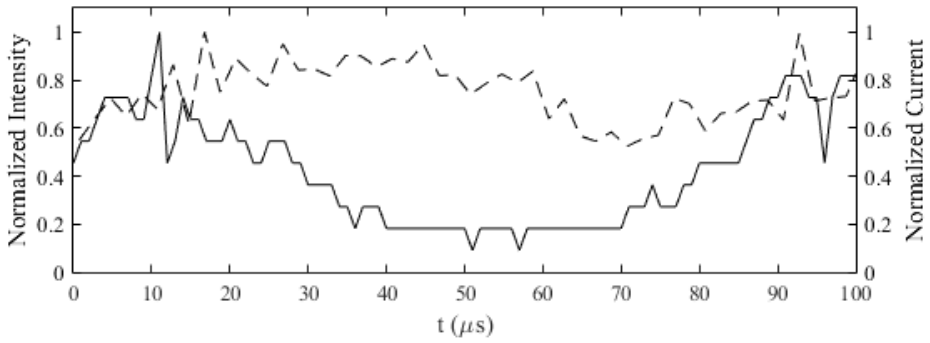

Figure A.29: Spoke mode test 3 magnetic and video data comparison. Solid line: video data. Dotted line: current data.

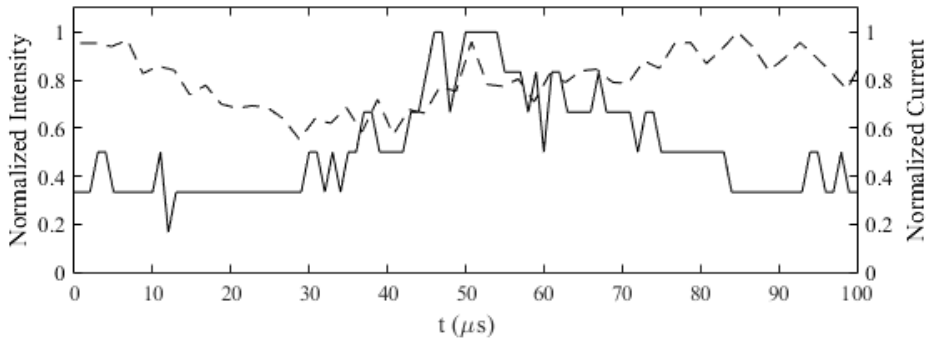

Figure A.30: Spoke mode test 5 magnetic and video data comparison. Solid line: video data. Dotted line: current data.

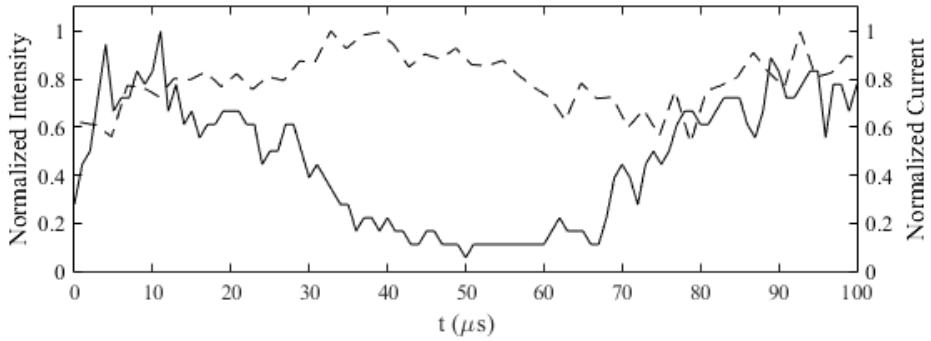

Figure A.31: Spoke mode test 6 magnetic and video data comparison. Solid line: video data. Dotted line: current data.

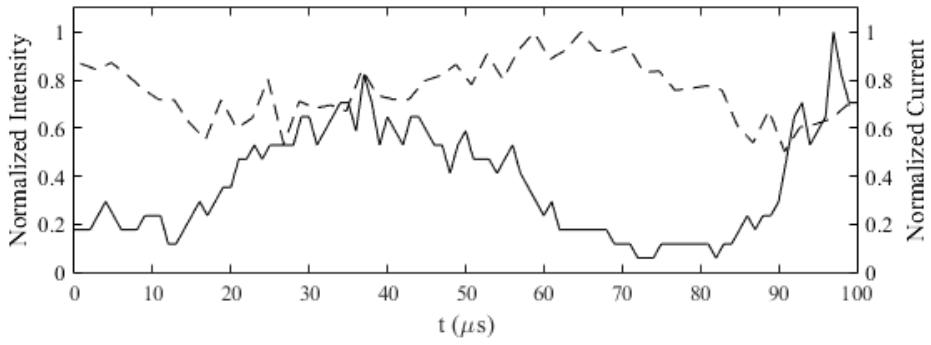

Figure A.32: Spoke mode test 7 magnetic and video data comparison. Solid line: video data. Dotted line: current data.

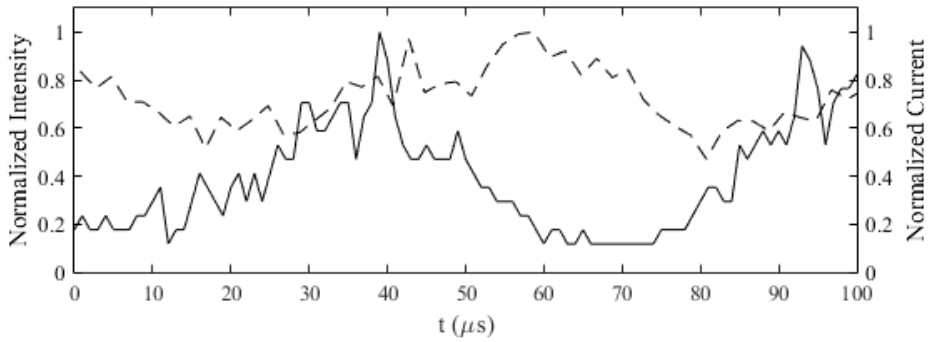

Figure A.33: Spoke mode test 8 magnetic and video data comparison. Solid line: video data. Dotted line: current data.

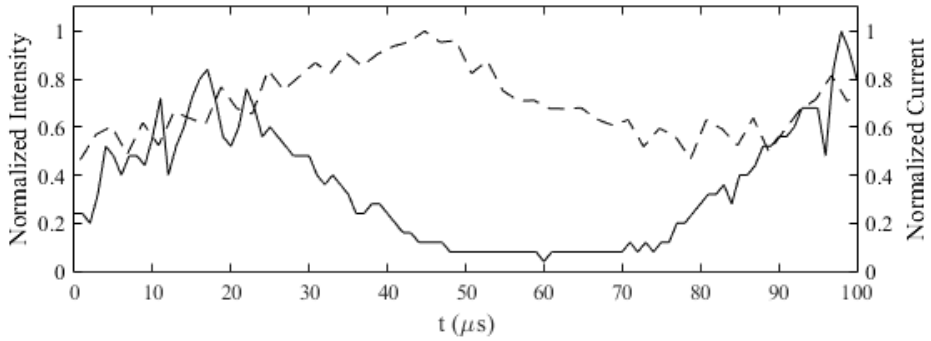

Figure A.34: Spoke mode test 10 magnetic and video data comparison. Solid line: video data. Dotted line: current data.

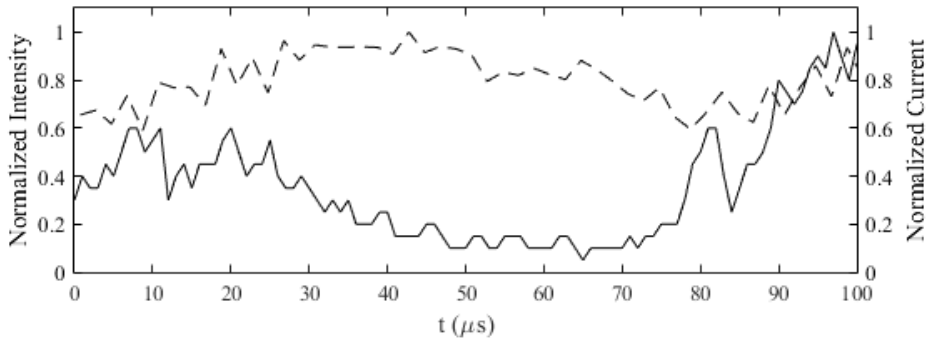

Figure A.35: Spoke mode test 12 magnetic and video data comparison. Solid line: video data. Dotted line: current data.

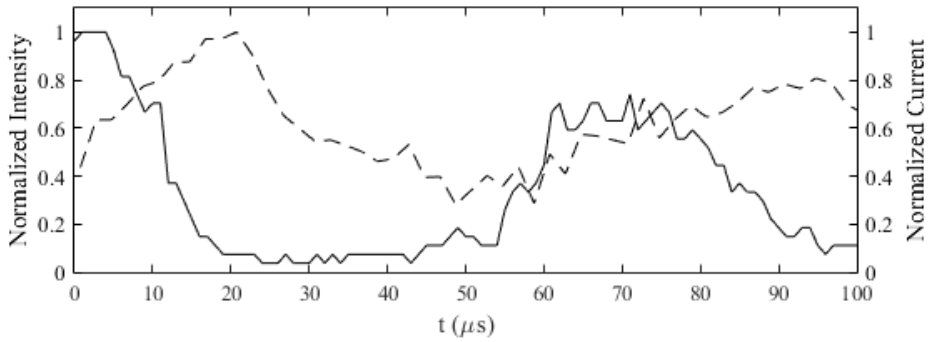

Figure A.36: Spoke mode test 15 magnetic and video data comparison. Solid line: video data. Dotted line: current data.

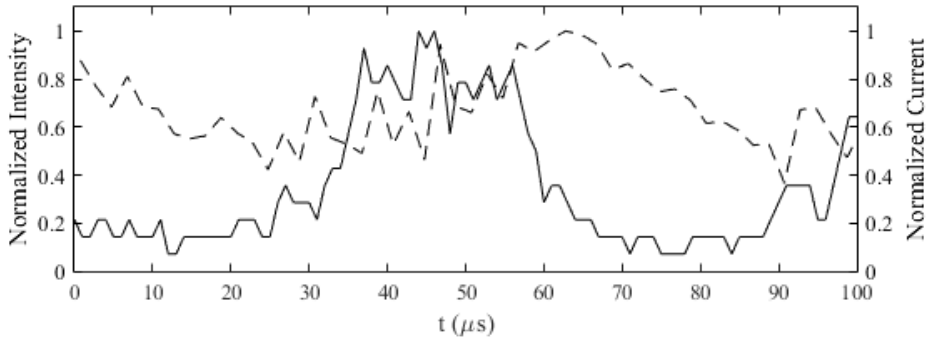

Figure A.37: Spoke mode test M-4 magnetic and video data comparison. Solid line: video data. Dotted line: current data.

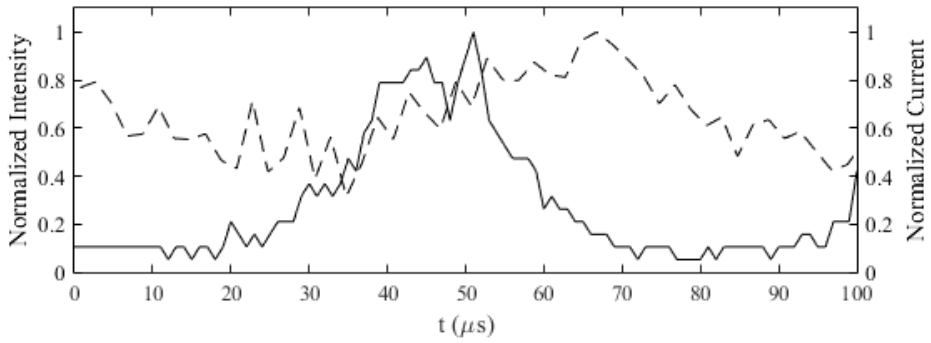

Figure A.38: Spoke mode test M-5 magnetic and video data comparison. Solid line: video data. Dotted line: current data.

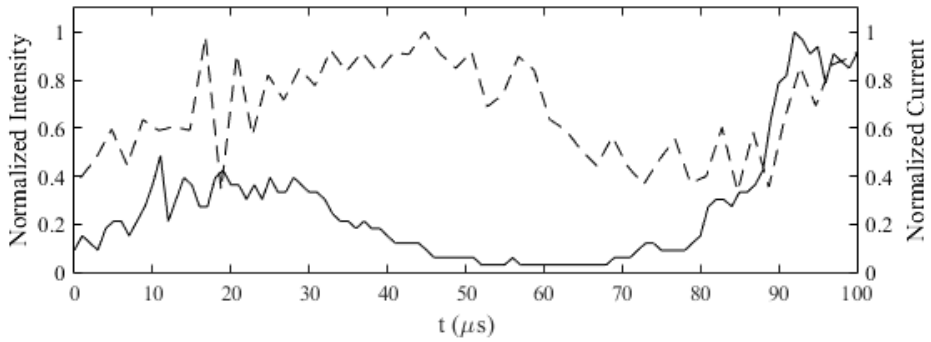

Figure A.39: Spoke mode test M-8 magnetic and video data comparison. Solid line: video data. Dotted line: current data.

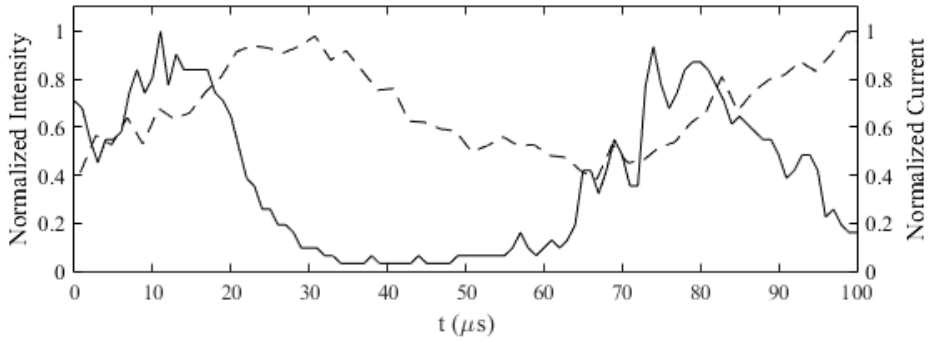

Figure A.40: Spoke mode test M-11 magnetic and video data comparison. Solid line: video data. Dotted line: current data.

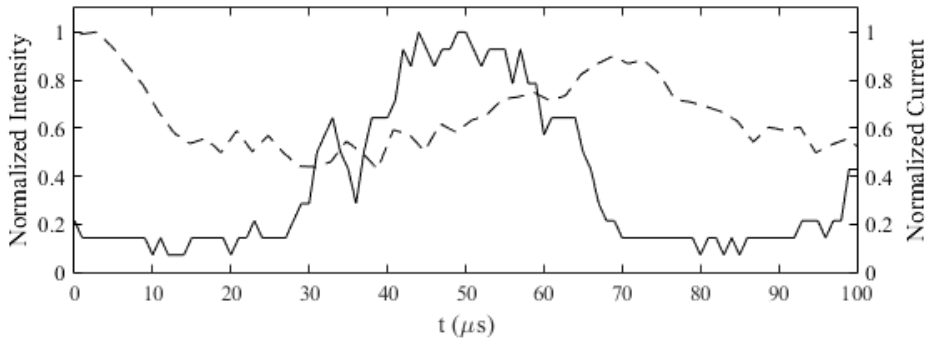

Figure A.41: Spoke mode test M-13 magnetic and video data comparison. Solid line: video data. Dotted line: current data.

Appendix B. Derivation of Relationship Between Spoke Velocity and Azimuthally Varying Potential, Eqs. 4.8 and 4.9

Assume spokes have a fixed azimuthal structure rotating with a constant velocity, like a wheel rotating around a hub. It is then possible to define a reference frame with azimuthal coordinate θ' so the potential $V'(\theta')$ has zero time derivative, but $dV'/d\theta'$ is nonzero in general. This reference frame is moving with respect to a reference frame fixed to the thruster or a sensor, with azimuthal coordinate θ and time coordinate t. By assumption frame θ' is moving with respect to frame θ with velocity $\dot{\theta}$, the spoke velocity. In the unprimed frame at a fixed azimuthal location a potential $V(t)$ is measured at an instant in time. The situation is illustrated in Fig. B.1 where the blue line is the spoke potential structure, fixed in the red primed frame. As seen in

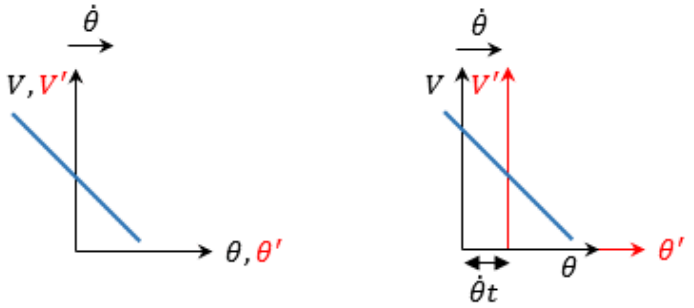

(a) At time $t = 0$ the frames coincide and $V = V'$.

(b) At time t, the red primed frame has translated right by a distance $\dot{\theta}t$ so $V(t) = V'(\theta') = V'(-\dot{\theta}t)$.

Figure B.1: Relationship between coordinate frames under consideration.

Fig. B.1(b), the potential measured at $\theta = 0$ in the unprimed frame is a potential at a different location in the primed frame $V'(\theta')$, where t and θ' are related by:

$$\theta' = -\dot{\theta}t. \tag{B.1}$$

This implies:

$$V(t) = V'(-\dot{\theta}t) \tag{B.2}$$

and it is seen Eq. B.2 is equivalent to Eq. 4.8. Next, consider the potential measured at a differentially incremented time $t + dt$. From Eq. B.2,

$$V(t + dt) = V'(-\dot{\theta}t - \dot{\theta}dt). \tag{B.3}$$

Because the spoke velocity is constant, it is seen from Eq. B.1:

$$d\theta' = -\dot{\theta}dt \tag{B.4}$$

so,

$$V(t + dt) = V'(\theta' + d\theta'). \tag{B.5}$$

Subtracting Eq. B.2 and dividing both sides by dt,

$$\frac{V(t + dt) - V(t)}{dt} = \frac{V'(\theta' + d\theta') - V'(\theta')}{dt} \tag{B.6}$$

but Eq. B.4 gave a relation from dt to $d\theta'$, so it is possible to write:

$$\frac{V(t + dt) - V(t)}{dt} = -\dot{\theta}\frac{V'(\theta' + d\theta') - V'(\theta')}{d\theta'}. \tag{B.7}$$

Now, since dt and $d\theta'$ are differential increments both the left and right hand sides of Eq. B.7 contain a derivative by definition and it is possible to write:

$$\frac{dV}{dt} = -\dot{\theta}\frac{dV'}{d\theta'} \tag{B.8}$$

or, rearranging,

$$\frac{dV'}{d\theta'} = -\frac{1}{\dot{\theta}}\frac{dV}{dt} \tag{B.9}$$

and it is seen Eq. B.9 is equivalent to Eq. 4.9.

Appendix C. Relevant Computer Code

C.1 Projected-Channel Plot Creation

The following three functions were used to create projected-channel plots from high-speed video images. Each video consisted of 102 .tif images.

C.1.1 Unwrapper.m.

```
% Projects an image of the channel of a Hall thruster onto several columns
% of pixels, interpolating the rows which are missing using natural nearest
% neighbor interpolation. Crops the output to only contain the channel.
% Written by: David Cunningham
% INPUT VARIABLES:
%   Image: Image, designed to be a 2-D matrix of uint8 values (intensities)
%      Other formats may cause issues.
%   r_in: Int, The column index of the first column of pixels that will be in
%   the output image.
%   r_out: Int, The column index of the last column of pixels that will be in
%   the output image.
%   center: [row col] Int, pixel coordinates of thruster center
%   Imsize: [row col] Int, size of image in pixels
% OUTPUT VARIABLES:
%   I: Image with dimension tres x (r_out-r_in), designed to be a 2-D
%   matrix of uint8 values.
%
% Use at own risk
function I = Unwrapper(Image, r_in, r_out, center, Imsize, emissive)
%%%%%%%%%%%% set image size and values %%%%%%%%%%

if emissive
   Image(184:196,151:162) = 1;
```

```
end
%~~~ BEGIN OMITTED CODE
% Adapted from URL: http://stackoverflow.com/a/12926591 and used
% under the Creative Commons Attribution Share Alike license at
% URL: https://creativecommons.org/licenses/by-sa/3.0/.
% Omitted to avoid publishing referenced code without appropriate
% license restrictions.
% END OMITTED CODE ~~~
% Convert to integers
Unroll = uint8(Unroll);
% crop
Unroll = imcrop(Unroll,[r_in, 0, r_out-r_in, 240]);
I = Unroll;
end
```

C.1.2 Unwrap_Video.m.

```
% Converts a Hall thruster video into a .tiff image with each column of
% pixels representing a frame in time (if averaging is true) and each row
% of pixels representing a set azimuthal location on the thruster channel
% (how big a section depends on the setup of Unwrapper.m). Saves image to
% video directory.
% INPUT VARIABLES:
%   WhichTest: STRING, designating which test in the series of tests to
%      use. This is a variable due to the need to convert many tests at
%      once (see Unwrap_All)
%   date: STRING, format 'YYYY_MM_DD', date of testing to go with file
%      folder structure convention.
%   averaging: BOOLEAN, if true averages all radial locations to one pixel.
%       If false, the output image is the entire channel projection from
```

```
%       each frame stacked with the inner channel wall of a frame touching
%       the outer wall of the previous frame.
% Written by: David Cunningham
% Use at own risk
function Unwrap_Video(WhichTest,date,averaging,emissive)
%%%%%%%%%%%%%%%%% Video Parameters %%%%%%%%%%%%%%%%
% To be set for each day of testing, or each time the camera is moved.
% It is recommended to fine tune these parameters with direct calls to
% Unwrapper.m using a test frame. Once the thruster channel appears as a
% straight line, input those values below.
chanIn  = 48; % first row of projected image to be cropped (inner channel radius)
chanOut = 60; % last row of projected image to be cropped (outer channel radius)
Xcenter = 158; % pixel coordinate of thruster center (column)
Ycenter = 124; % pixel coordinate of thruster center (row)

%%%%%%%%%%%%%%%% Initialize Variables %%%%%%%%%%%%%
oldDir = cd(strcat('INSERT FOLDER PATH',date,'\TIFF\Test_',WhichTest,'_Video'));
testsize = Unwrapper(imread(strcat('Test_',WhichTest,'_Video_',...
           num2str(1,'%03i'),'.tiff')), chanIn,chanOut,[Ycenter,Xcenter],...
           [260,312],emissive);
Images = uint8(zeros(size(testsize,1),size(testsize,2),102));
if averaging
   BigPicture = uint8(zeros(size(testsize,1),102));
   avgstring = 'Pixels_condensed';
else
   avgstring = 'Full_Width';
end

%%%%%%%%%%%%%%% Read in each frame, unroll it, add it to output image %%%%
```

```
for i = 1:102
   % note the image may have gain applied here.
   Images(:,:,i) = Unwrapper(imread(strcat('Test_',WhichTest,'_Video_',...
   num2str(i,'%03i'),'.tiff')),chanIn,chanOut,[Ycenter,Xcenter],[260,312],emissive);
   if ~averaging
      if i == 1
         for j = 1:size(Images,1)
            BigPicture(j,:,1) = uint8(Images(j,:,i));
         end
      else
         for j = 1:size(Images,1)
            holder(j,:) = uint8(Images(j,:,i));
         end
         BigPicture = [BigPicture holder];
      end
   elseif averaging
      for j = 1:size(Images(:,1,1))
         BigPicture(j,i) = uint8(mean2(Images(j,:,i)));
      end
   end
end

%%%%%%%%%%%%%%% Display and Save %%%%%%%%%%%%%
imshow(BigPicture)
imwrite(BigPicture, strcat('Test_',WhichTest,'_Unrolled_',avgstring,'.tiff'));
cd(oldDir);
```

C.1.3 Make_Surface_From_Unrolled.m.

```
% create surface plot from unrolled video, set up for 1Mfps, 2 deg/pixel
% INPUT VARIABLES:
%   WhichTest: STRING, designating which test in the series of tests to
%      use. This is a variable due to the need to convert many tests at
%      once
%   date: STRING, format 'YYYY_MM_DD', date of testing to go with file
%      folder structure convention.
%   save: BOOLEAN, if true saves output image to .fig file
%   color: BOOLEAN, if true uses Matlab hot colormap on surface
%   gain: Int, gain multiple to apply to output
% Written by: David Cunningham
% Maintained by: David Cunningham
% Use at own risk
function Make_Surface_From_Unrolled(WhichTest,date,save,color, gain)
% WhichTest = '10';
oldDir = cd(strcat('INSERT FOLDER PATH',WhichTest,'_Video'));
I = gain*imread(strcat('Test_',WhichTest,'_Unrolled_Pixels_condensed.tiff'));
surf(I,'EdgeColor','none');
view(2);
array = 0:0.01:1;
map = [array;array;array];
colormap(map')
xlim([1,102]);
ylim([1,180]);
ax = gca;
ax.XTick = [11:10:101];
ax.XTickLabel = {'10','20','30','40','50','60','70','80','90','100'};
ax.YTick = [1,45,90,135,180];
```

```
ax.YTickLabel = {'-180','-90','0','90','180'};
xlabel('time (\mus)');
ylabel('Azimuthal position (deg)');
if color
   colormap hot
end
% title(strcat('Test ',WhichTest,' \Theta vs. t Plot'));
if save
   cd(strcat('E:\Research Data\Analyzed Data\',date,'\PC Plots'));
   savefig(strcat('Unrolled_Plot_',WhichTest));
   print(strcat('Unrolled_Plot_',WhichTest),'-dtiff');
end

cd(oldDir)
```

C.2 Spoke_Velocity_Tool.m

This program was used to obtain the velocity of azimuthal spokes by translating pixel columns until spokes appeared as horizontal lines.

```
% Spoke Velocity Tool
% Written by David Cunningham
WhichTest = 'F'; % replace with test number
gain = 5;

I = gain*imread(''); % insert location of projected-channel plot to be analyzed
go = true;
surf(I,'EdgeColor','none');
view(2);
xlim([1,102]);
ylim([1,180]);
```

```
colormap hot
dt = input('time region? >>');

figure
offset = 0;

while go
   pix = offset;
   offset = input('pixel offset >> ');
   if offset == 'q'
      go = false;
      break
   end
   for i = 1:size(I,2)
      if offset >=0
         topPad(i) = abs(offset)*(i-1);
         bottomPad(i) = abs(offset)*(size(I,2)-(i-1));
      elseif offset <0
         topPad(i) = abs(offset)*(size(I,2)-(i-1));
         bottomPad(i) = abs(offset)*(i-1);
      end
      skewImage(:,i) = [uint8(zeros(topPad(i),1)); I(:,i);...
                        uint8(zeros(bottomPad(i),1))];
   end
   gcf;
   surf(skewImage,'EdgeColor','none');
   axis square;
   view(2);
   title(strcat('Skew = ',num2str(offset)));
```

```
   xlim([dt(1),dt(2)]);
   figtop = find(skewImage(:,floor(mean(dt)))>0,1,'last');
   figbot = find(skewImage(:,floor(mean(dt)))>0,1,'first');
   ylim([figbot,figtop]);
   colormap hot
   clear skewImage
end

secsperRev = abs(360*1e-6/(2*pix));
freq = 1/secsperRev;
disp(strcat('Spoke Frequency: ',num2str(freq),' Hz.'));
```

Bibliography

1. Goebel, D. M. and Katz, I., *Fundamentals of Electric Propulsion*, No. 1 in JPL Space Science and Technology Series, Wiley, Hoboken, New Jersey, 2008.

2. Busek Co. Inc., "Busek's Hall Effect Thruster Technology saves Air Force AEHF satellite," 2012.

3. Sellers, J. J., *Understanding Space*, Space Technology Series, McGraw Hill, New York, New York, 3rd ed., 2005.

4. Chen, F. F., *Introduction to Plasma Physics*, Plenum, New York, New York, 1974.

5. Griffiths, D. J., *Introduction to Electrodynamics*, Pearson, Boston, Massachusetts, 4th ed., 2013.

6. Ellison, C. L., Raitses, Y., and Fisch, N. J., "Cross-field Electron Transport Induced by a Rotating Spoke in a Cylindrical Hall Thruster," *Physics of Plasmas*, Vol. 19, 2012, pp. 013503–1 – 013503–7.

7. Raitses, Y., Griswold, M., Ellison, L., Parker, J., and Fisch, N. J., "Studies of Rotating Spoke Oscillations in Cylindrical Hall Thrusters," *48th AIAA/ASME/SAE/ASEE Joint Propulsion Conference & Exhibit*, Atlanta, Georgia, 2012.

8. Tang, D. L., Geng, S. F., Qiu, X. M., and Chu, P. K., "Three-dimensional Numerical Investigation of Electron Transport with Rotating Spoke in a Cylindrical Anode Layer Hall Plasma Accelerator," *Physics of Plasmas*, Vol. 19, 2012, pp. 073519–1 – 013503–4.

9. Sekerak, M. J., *Plasma Oscillations and Operational Modes in Hall Effect Thrusters*, Ph.D. thesis, University of Michigan, Ann Arbor, Michigan, 2014.

10. Goebel, D. M., Hofer, R. R., Mikellides, I. G., Katz, I., Polk, J. E., and Dotson, B. N., *Conducting Wall Hall Thrusters*, Vol. 43, 2015.

11. Zhurin, V. V., Kaufman, H. R., and Robinson, R. S., "Physics of Closed Drift Thrusters," *Plasma Sources Sci. Technol.*, Vol. 8, 1999, pp. R1 – R20.

12. Janes, G. S. and Lowder, R. S., "Anomalous Electron Diffusion and Ion Acceleration in a Low-Density Plasma," *Physics of Fluids*, Vol. 9, No. 6, June 1966, pp. 1115–1123.

13. Esipchuk, Y. B., Morozov, A. I., Tilinin, G. N., and Trofimov, A. V., "Plasma oscillations in closed-drift accelerators with an extended acceleration zone," *Sov. Phys. Tech. Phys.*, Vol. 18, No. 7, January 1973, pp. 928–932.

14. Meezan, N. B., Hargus, W. A. J., and Cappelli, M. A., "Anomalous Electron Mobility in a Coaxial Hall Discharge Plasma," *Physical Review E*, Vol. 63, 2001, pp. 026410–1 – 026410–7.

15. Morozov, A. I., "Wall Conduction in a Highly Magnetized Plasma," *Journal of Applied Mechanical and Technical Physics*, Vol. 9, No. 3, 1968, pp. 19 – 22.

16. Yoshikawa, S. and Rose, D. J., "Anomalous Diffusion of a Plasma across a Magnetic Field," *Physics of Fluids*, Vol. 5, No. 3, March 1962, pp. 334–340.

17. Raitses, Y., Staack, D., Keidar, M., and Fisch, N. J., "Electron-Wall Interaction in Hall Thrusters," *Physics of Plasmas*, Vol. 12, 2005, pp. 057104–1 – 057104–9.

18. Gascon, N., Dudeck, M., and Barral, S., "Wall Material Effects in Stationary Plasma Thrusters," *Physics of Plasmas*, Vol. 10, No. 10, 2003, pp. 4123 – 4136.

19. Barral, S., Makowski, K., Peradzyński, Z., and Dudeck, M., "Is Near-Wall Conductivity a Misnomer?" *39th Joint Propulsion Conference and Exhibit*, Huntsville, Alabama, July 2003.

20. Ivanov, A. A., Ivanov, A. A. J., and Bacal, M., "Effects of Plasma-Wall Recombination on the Conductivity in Hall Thrusters," *Plasma Physics and Controlled Fusion*, Vol. 44, 2002, pp. 1463 – 1470.

21. Garrigues, L., Hagelaar, G. J. M., Boniface, C., and Boeuf, J. P., "Anomalous Conductivity and Secondary Electron Emission in Hall Effect Thrusters," *Journal of Applied Physics*, Vol. 100, 2006, pp. 123301–1 – 123301–9.

22. Boniface, C., Garrigues, L., Hagellar, G. J. M., Boeuf, J. P., Gawron, D., and Mazouffre, S., "Anomalous Cross Field Electron Transport in a Hall Effect Thruster," *Applied Physics Letters*, Vol. 89, 2006, pp. 161503–1 – 161503–3.

23. Choueiri, E. Y., "Plasma oscillations in Hall thrusters," *Physics of Plasmas*, Vol. 8, No. 4, April 2001, pp. 1411–1426.

24. Boeuf, J.-P. and Garrigues, L., "Low frequency oscillations in a stationary plasma thruster," *Journal of Applied Physics*, Vol. 84, 1998, pp. 3541.

25. Fife, J. M., Martinez-Sanchez, M., and Szabo, J., "A Numerical Study of Low-Frequency Discharge Oscillations in Hall Thrusters," Tech. Rep. AIAA-97-3051, American Institute of Aeronautics and Astronautics, Washington, D. C., 1997.

26. Smith, A. W. and Cappelli, M. A., "Time and space-correlated plasma potential measurements in the near field of a coaxial Hall plasma discharge," *Physics of Plasmas*, Vol. 16, 2009.

27. Kurzyna, J., Mazouffre, S., Lazurenko, A., Albarède, L., Bonhomme, G., Makowski, K., Dudeck, M., and Peradzyński, "Spectral analysis of Hall-effect thruster plasma oscillations based on the empirical mode decomposition," *Physics of Plasmas*, Vol. 12, 2005.

28. Liu, D., Huffman, R. E., Branam, R. D., and Hargus, W. A., "Ultrahigh Speed Images of Hall Thruster Azimuthal Instabilities," *IEEE Transactions on Plasma Science*, Vol. 42, No. 10, 2014, pp. 2656 – 2657.

29. McDonald, M. S. and Gallimore, A. D., "Rotating Spoke Instabilities in Hall Thrusters," *IEEE Transactions on Plasma Science*, Vol. 39, No. 11, 2011, pp. 2952 – 2953.

30. Escobar, D. and Ahedo, E., "Low frequency azimuthal stability of the ionization region of the Hall thruster discharge. I. Local analysis," *Physics of Plasmas*, Vol. 21, 2014.

31. Escobar, D. and Ahedo, E., "Global Stability Analysis of Azimuthal Oscillations in Hall Thrusters," *IEEE Transactions on Plasma Science*, Vol. 43, No. 1, January 2015, pp. 149–157.

32. Lam, C. M., Ferndandez, E., and Cappelli, M. A., "A 2-D Hybrid Hall Thruster Simulation That Resolves the $\mathbf{E}\times\mathbf{B}$ Electron Drift Direction," *IEEE Transactions on Plasma Science*, Vol. 43, No. 1, January 2015, pp. 86–94.

33. Kemp, R. F. and Sellen, J. M. J., "Plasma Potential Measurements by Electron Emissive Probes," *Review of Scientific Instruments*, Vol. 100, 1966, pp. 455–461.

34. Mullins, C. R., Martinez, R. A., Williams, J. D., Farnell, C. C., Farnell, C. C., Liu, D., and Branam, R. D., "Non-Invasive Hall Current Distribution Measurement in a Hall Effect Thruster," *The 51st AIAA/SAE/ASEE Joint Propulsion Conference*, No. AIAA 2015-4005, Orlando, Florida, July 2015.

35. Hershkowitz, N. and Cho, M. H., "Measurement of Plasma Potential Using Collecting and Emitting Probes," *Journal of Vacuum Science and Technology A*, Vol. 9, 1988, pp. 2054 – 2059.

36. Sheehan, J. P., Raitses, Y., and Hershkowitz, N., "Accurately Determining the Plasma Potential Using Emissive Probes," *The 33rd International Electric Propulsion Conference*, Washington, D.C., October 2013.

37. Mazouffre, S., Pétin, A., Kudrna, P., and Tichý, M., "Development of a High-Frequency Emissive Probe System for Plasma Potential Measurements in a Hall Thruster," *IEEE Transactions on Plasma Science*, Vol. 43, 2015, pp. 29 – 34.

38. Rubin, B., Kapulkin, A., and Guelman, M., "Research on Optimization of Onboard Magnetic Diagnostics System of Hall Thruster Plasma," *The 29th International Electric Propulsion Conference*, Princeton, New Jersey, October 2005.

39. Rubin, B., *Analysis and Numerical Experimentation of Onboard Diagnostic Systems for Hall Thrusters*, Ph.D. thesis, Technion-Israel Institute of Technology, Haifa, Israel, 2006.

40. Liu, D., *Two-Dimensional Time-Dependent Plasma Structures of a Hall Effect Thruster*, Ph.D. thesis, Air Force Institute of Technology, Wright-Patterson Air Force Base, Ohio, September 2011.

41. Yamamoto, N., Komurasaki, K., and Arakawa, Y., "Discharge current oscillation in Hall thrusters," *Journal of propulsion and power*, Vol. 21, No. 5, 2005, pp. 870–876.

42. Sekerak, M. J., Longmier, B. W., Gallimore, A. D., Brown, D. L., Hofer, R. R., and Polk, J. E., "Azimuthal Spoke Propagation in Hall Effect Thrusters," *The 33rd International Electric Propulsion Conference*, Washington, D.C., October 2013.

Vita

Captain David A. Cunningham attended the University of Texas at Austin where he earned a Bachelor of Science degree in Aerospace Engineering in May 2011. While studying at UT he was a member of Air Force ROTC Detachment 825 and he recieved his commission in the Air Force upon graduation. His first assignment was as a developmental engineer in the 17$^{\text{th}}$ Test Squadron at Schriever AFB, CO where he was responsible for planning and executing operational tests of various Air Force Space Command systems. In August 2014 he entered the Graduate School of Engineering and Management at the Air Force Institute of Technology. After graduating he will be an instructor in the Department of Astronautics at the United States Air Force Academy in Colorado Springs.

Permanent address: 2950 Hobson Way
Air Force Institute of Technology
Wright-Patterson AFB, OH 45433

REPORT DOCUMENTATION PAGE

Form Approved
OMB No. 0704–0188

1. REPORT DATE *(DD–MM–YYYY)*	2. REPORT TYPE	3. DATES COVERED *(From — To)*
04–03–2016	Master's thesis	Aug 2014–Mar 2016

4. TITLE AND SUBTITLE

Localized Plasma Measurement During Instability Modes In a Hall Thruster

5a. CONTRACT NUMBER

5b. GRANT NUMBER

5c. PROGRAM ELEMENT NUMBER

6. AUTHOR(S)

Cunningham, David A., Captain, USAF

5d. PROJECT NUMBER

5e. TASK NUMBER

5f. WORK UNIT NUMBER

7. PERFORMING ORGANIZATION NAME(S) AND ADDRESS(ES)

Air Force Institute of Technology
Graduate School of Engineering and Management (AFIT/EN)
2950 Hobson Way
WPAFB, OH 45433-7765

8. PERFORMING ORGANIZATION REPORT NUMBER

AFIT-ENY-MS-16-M-203

9. SPONSORING / MONITORING AGENCY NAME(S) AND ADDRESS(ES)

Air Force Office of Scientific Research Energy, Power and Propulsion Directorate
Attn: Dr. Mitat Birkan
875 N. Randolph, Ste 325
Arlington, VA 22203
mitat.birkan@us.af.mil

10. SPONSOR/MONITOR'S ACRONYM(S)

AFOSR/RTE

11. SPONSOR/MONITOR'S REPORT NUMBER(S)

12. DISTRIBUTION / AVAILABILITY STATEMENT

DISTRIBUTION STATEMENT A. APPROVED FOR PUBLIC RELEASE; DISTRIBUTION IS UNLIMITED. This material is declared a work of the U.S. Government and is not subject to copyright protection in the United States.

13. SUPPLEMENTARY NOTES

The views expressed in this thesis are those of the author and do not reflect the official policy or position of the United States Air Force, the Department of Defense, or the United States Government.

14. ABSTRACT

Hall thrusters are a key technology for current and future unmanned satellites, striking a balance between thrust and fuel economy suitable for many mission profiles of interest. Despite their extensive flight heritage and a large body of research, many phenomena occuring in the plasma discharge of Hall thrusters are not well understood. A combination of intrusive and non-intrusive measurement techniques were used to investigate the properties of the exhaust plume of two Hall thrusters and correlate optical characteristics of oscillating modes with the plasma potential and azimuthal current distribution during those modes. A strong trend was found associating the optical emission of spokes with a local increase in plasma potential as measured by an emissive probe, indicating a spoke structure with visible and non-visible regions. Additionally, a consistent phase delay was observed between oscillations in discharge current and Hall current during the breathing mode. A similar delay was not observed between discharge current and optical emission or plasma potential oscillations during the breathing mode. These trends were used to infer a possible plasma structure during breathing and spoke modes.

15. SUBJECT TERMS

Hall thrusters; Hall effect thrusters; electric propulsion; rocket propulsion; plasma physics; plasma diagnostics; plasma instabilities

16. SECURITY CLASSIFICATION OF:			17. LIMITATION OF ABSTRACT	18. NUMBER OF PAGES	19a. NAME OF RESPONSIBLE PERSON
a. REPORT	b. ABSTRACT	c. THIS PAGE			Dr. Carl Hartsfield, AFIT/ENY
U	U	U	UU	112	19b. TELEPHONE NUMBER *(include area code)* (937)255-3636 x4667 carl.hartsfield@afit.edu